USGS
science for a changing world

هيئة المساحة الجيولوجية السعودية
SAUDI GEOLOGICAL SURVEY

Cenozoic Tectonics of the Western Arabia Plate Related to Harrat Magmatism near Al Madīnah, Kingdom of Saudi Arabia

Chapter B of
Active Volcanism on the Arabian Shield—Geology, Volcanology, and Geophysics of Northern Harrat Rahat and Vicinity, Kingdom of Saudi Arabia

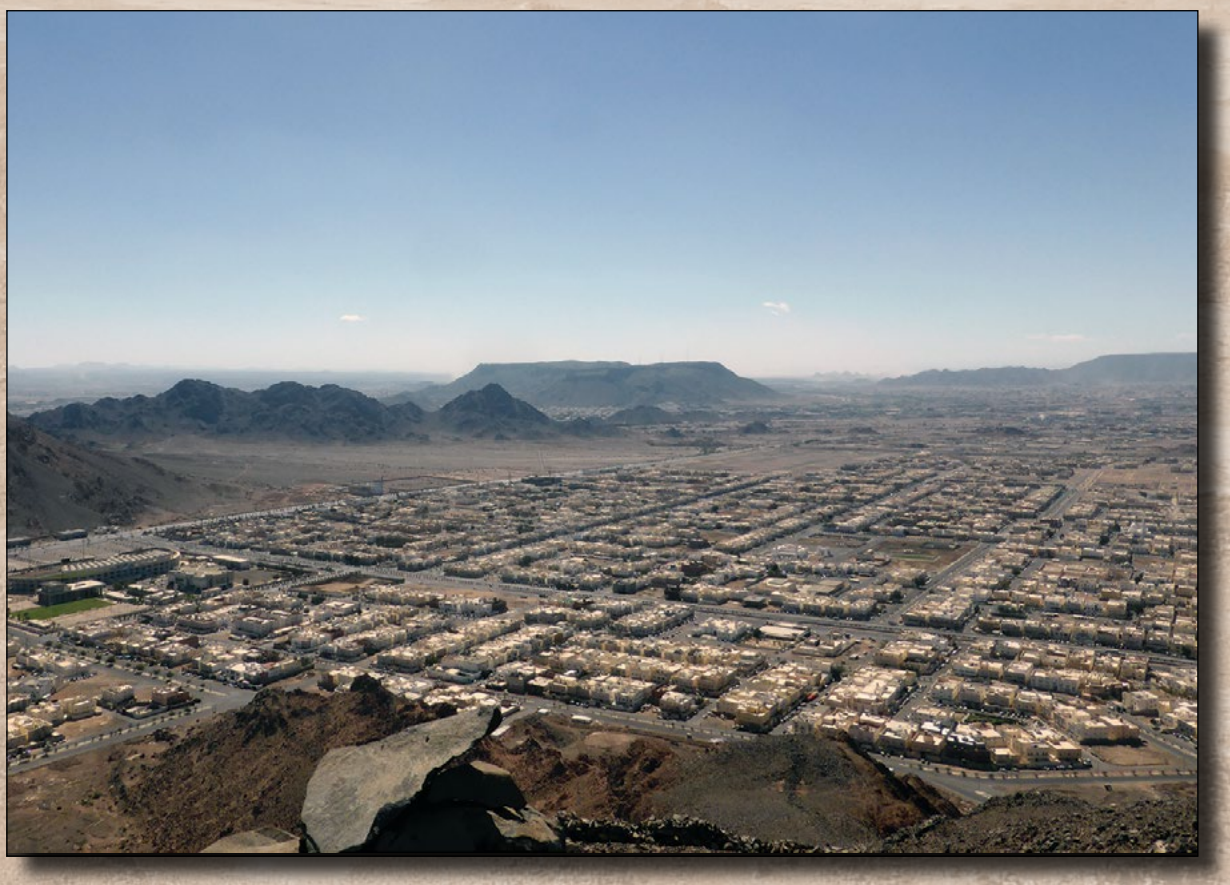

U.S. Geological Survey Professional Paper 1862
Saudi Geological Survey Special Report SGS–SP–2021–1

U.S. Department of the Interior
U.S. Geological Survey

Cover. Photograph showing Proterozoic metamorphic and plutonic rocks of the Arabian Shield exposed in the rugged topography of low hills and lower parts of flat-topped hills south of Al Madīnah and west of Harrat Rahat. Subdued topography of upper Jabal Jimmah (left) and Jabal ʻAyr (center with telecommunication towers) consist of Miocene, pre-Harrat Rahat lava flows that unconformably overlie the Arabian Shield rocks. Hills were either uplifted by now-obscured faults, or were incised relative to the basin that hosts Harrat Rahat, after deposition of the Miocene lavas. Harrat Rahat lava domes are visible on the skyline between Jabal ʻAyr and Jabal Jimmah. View is to the south-southeast from the As Salam district in the western suburb of Al Madīnah. U.S. Geological Survey photograph by A. Calvert on February 20, 2015. Background image shows northern Harrat Rahat lava flows, maars, and lava domes. U.S. Geological Survey photograph by Andrew Calvert, January 25, 2012.

Cenozoic Tectonics of the Western Arabia Plate Related to Harrat Magmatism near Al Madīnah, Kingdom of Saudi Arabia

By Andrew T. Calvert and Thomas W. Sisson

Chapter B of

Active Volcanism on the Arabian Shield—Geology, Volcanology, and Geophysics of Northern Harrat Rahat and Vicinity, Kingdom of Saudi Arabia

Edited by Thomas W. Sisson, Andrew T. Calvert, and Walter D. Mooney

U.S. Geological Survey Professional Paper 1862
Saudi Geological Survey Special Report SGS–SP–2021–1

U.S. Department of the Interior
U.S. Geological Survey

U.S. Geological Survey, Reston, Virginia: 2023

For more information on the USGS—the Federal source for science about the Earth, its natural and living resources, natural hazards, and the environment—visit https://www.usgs.gov or call 1–888–ASK–USGS.

For an overview of USGS information products, including maps, imagery, and publications, visit https://store.usgs.gov.

Suggested citation:
Calvert, A.T., and Sisson, T.W., 2023, Cenozoic tectonics of the western Arabia Plate related to harrat magmatism near Al Madīnah, Kingdom of Saudi Arabia, chap. B *of* Sisson, T.W., Calvert, A.T., and Mooney, W.D., eds., Active volcanism on the Arabian Shield—Geology, volcanology, and geophysics of northern Harrat Rahat and vicinity, Kingdom of Saudi Arabia: U.S. Geological Survey Professional Paper 1862 [also released as Saudi Geological Survey Special Report SGS–SP–2021–1], 28 p., https://doi.org/10.3133/pp1862B.

ISSN 1044-9612 (print)
ISSN 2330-7102 (online)

هيئة المساحة الجيولوجية السعودية
SAUDI GEOLOGICAL SURVEY

Ministry of Industry and Mineral Resources
BANDAR BIN IBRAHIM BIN ABDULLAH AL-KHORAYEF, Minister and SGS Chairman

Saudi Geological Survey
Abdullah bin Mufter Al-Shamrani, Chief Executive Officer

Saudi Geological Survey, Jiddah, Kingdom of Saudi Arabia: 2023

Contents

Figures

Tables

Conversion Factors

International System of Units to U.S. customary units

Multiply	By	To obtain
	Length	
meter (m)	3.281	foot (ft)
meter (m)	1.094	yard (yd)
kilometer (km)	0.6214	mile (mi)
	Area	
square kilometer (km^2)	247.1	acre
square kilometer (km^2)	0.3861	square mile (mi^2)
	Volume	
cubic kilometer (km^3)	0.2399	cubic mile (mi^3)
	Flow rate	
millimeter per year (mm/yr)	0.03937	inch per year (in/yr)

Temperature in degrees Celsius (°C) may be converted to degrees Fahrenheit (°F) as follows:

$$°F = (1.8 \times °C) + 32.$$

Abbreviations

C.E.	Common Era
GPS	Global Positioning System
ka	kilo-annum
Ma	mega-annum
MORB	midocean ridge basalt
SGS	Saudi Geological Survey
USGS	U.S. Geological Survey

Active Volcanism on the Arabian Shield
Edited by T.W. Sisson, A.T. Calvert, and W.D. Mooney
U.S. Geological Survey Professional Paper 1862
Saudi Geological Survey Special Report SGS–SP–2021–1

Chapter B

Cenozoic Tectonics of the Western Arabia Plate Related to Harrat Magmatism near Al Madīnah, Kingdom of Saudi Arabia

By Andrew T. Calvert and Thomas W. Sisson

Abstract

Sprawling volcanic fields, or harrats, in western Saudi Arabia have been emplaced during the past 30 million years following effusions of flood basalts in Ethiopia and Yemen. Although broadly associated with volcanism in three rift valleys (Red Sea, Gulf of Aden, and East African Rift Zone) radiating from the Afar depression, harrat abundance on the Arabian Peninsula indicates that volcanism is distinct from processes that opened the Red Sea and drive its magmatism. Harrats primarily lie unconformably on the Arabian Shield and locally on Paleozoic platform deposits, but several are conformable upon or interbedded with Paleogene supracrustal strata. Harrats erupted from linear chains of vents; some are oriented parallel to the Red Sea (N. 30° W.), but most trend northerly or north-northeasterly. Harrats consist mainly of weakly alkalic basalts and lesser amounts of their differentiation products, but some contain strongly alkalic rocks such as basanites and phonolites. Early harrats predate initial opening of the Red Sea 24–20 million years ago (Ma) and uplift of its flank 20–11 Ma, but younger harrats postdate the uplift and are larger and more abundant. Seismic studies identify substantially thinned continental lithosphere beneath the most voluminous harrats, but little crustal thinning is apparent at the surface, an indication that the lithosphere was eroded from below. The combination of plume impingement, rift valley formation, and erosion of the lithosphere beneath the Arabian Shield since 30 Ma indicates that the Afar plume thermally weakened the region, enabling the Arabia Plate to separate from the Africa Plate along the Red Sea and Gulf of Aden. The plume also thinned interior parts of the newly formed Arabia Plate, not just its margins, promoting mantle melting and volcanism.

Introduction

Harrats in the Kingdom of Saudi Arabia are large, predominantly mafic, coalescing volcanic fields that lie near the west edge of the Arabia Plate. Depending on how the coalescing fields are divided, there are more than 18 volcanic fields (table 1) on the east side of the Red Sea, compared with only 7 small fields on the west side (figs. 1 and 2). All harrats are 30 million years old (Ma) or younger, and most are younger than 10 Ma. Many were active during the Pleistocene or Holocene. The causative processes of harrat volcanism are poorly known, with little agreement among published studies. The region is undergoing extension, manifested by the young Red Sea, Gulf of Aden, and Afar depression, but continental crust in the vicinity of the harrats is only weakly extended. The frequency, timing, and volume of volcanism is asymmetric on opposite sides of the Red Sea. Arrival of a mantle plume is widely accepted as having produced flood basalts in Ethiopia, Sudan, and Yemen and weakened the lithosphere, leading to continental breakup; but harrats are not larger approaching the plume center nor evenly distributed around it, so a plume source is far from certain for harrat magmatism. This report summarizes advances in the understanding of the tectonic history of the region, drawing from the published literature, theses, and limited new field observations. New geologic mapping (Downs and others, 2019; Robinson and Downs, 2023) and five new $^{40}Ar/^{39}Ar$ ages on lavas constrain understanding of the timing and nature of some of these tectonic events and are presented herein. Possible tectonic and magmatic models for the origins of harrat volcanism are then evaluated.

Importance and Complexities of Red Sea Tectonics

The Red Sea, Gulf of Aden, and East African Rift Zone are prototypical examples in continental rifting that were followed by oceanic spreading in the Red Sea and Gulf of Aden. The rifts meet at the Afar depression, a triple junction that is inferred to have formed in response to the Afar Hot Spot plume, whose arrival at about 30 Ma was heralded by eruptions of flood basalts that blanket much of the Ethiopian highlands, southeastern Sudan, and western Yemen. Rifting, dike emplacement from Yemen to the Sinai Peninsula, plate separation, and subsidence at the triple junction followed flood basalt volcanism, as did uplift of continental crust adjacent

Table 1. Selected Saudi Arabian volcanic fields (harrats), alternate names, radiometric ages, and associated references.

[Arranged from north to south. See figure 1 for map of those volcanic fields mentioned in this study. Harrats with undated but young-appearing lava flows indicated by "recent" age. Ma, mega-annum]

Harrat name (this study)	Name from Brown and others (1989)	Alternate name	Notes	Age range	References
Harrat ash Shamā	Al Harrah	Harrat ash Shāmah, Harrat Shama, Harrat ash Shaam		27–22, 16–1 Ma, 0.8–0.1 Ma	Brown and others, 1989; Coleman, 1993; Ilani and others, 2001; Bosworth and Stockli, 2016
Harrat ar Rahá	Ḥarrat ar Raḥāh-'Uwayrid		Northern extent of Harrat al 'Uwayrid	9.5 Ma to recent	Brown and others, 1989; Coleman, 1993
Harrat al 'Uwayrid	Ḥarrat ar Raḥāh-'Uwayrid		Southern extent of Harrat ar Rahá	9.5 Ma to recent	Brown and others, 1989; Coleman, 1993
Harrat al Hutaymah				1.8 Ma	Pallister, 1984
Harrat Ithnayn	Ḥarrat al Ithnayn, Harrat Hutaym	Ḥarrat Hutaym		3 Ma to recent	Camp and others, 1991
Harrat Harairah	Ḥarrat Harairah		Fills Hamd-Jizl basin, analogous to Ḥarrat I'shara-Khirsat	17–12 Ma (63–21 Ma and 11–7 Ma dates listed by Brown and others, 1989, appear unreliable)	Coleman, 1993
Harrat Khaybar	Ḥarrat Khaybar			5 Ma to recent	Camp and others, 1991
Harrat Kurá	Ḥarrat al Kūrá	Harrat Kura		11.5–5 Ma	Brown and others, 1989; Coleman, 1993; Camp and others, 1991
Harrat Lunayyir	Ḥarrat Lunayyir			1–0.5 Ma	Brown and others, 1989; Coleman, 1993
Harrat I'shara-Khirsāt	Ḥarrat I'shara-Khirsāt		Fills Hamd-Jizl basin, analogous to Ḥarrat Harairah	17–12 Ma (63–21 Ma and 11–7 Ma dates listed by Brown and others, 1989, appear unreliable)	Brown and others, 1989; Szymanski, 2013
Harrat Kuramā'	Ḥarrat Kuramā'			20 Ma	Brown and others, 1989
Not used	Ḥarrat an Nabah				
Harrat Rahat	Ḥarrat Rahat		Harrat Rahat includes Harrat Rashid (also known as Harrat al Madīnah), Harrat Bani Abdullah, Harrat Turrah, and Harrat ar Rukhq (see below)	10 Ma to recent	Camp and Roobol, 1989, 1991; Brown and others, 1989
Harrat Rashid	Ḥarrat abu Rashid		Same as Harrat al Madīnah	1.2 Ma to recent	Camp and Roobol, 1989; Brown and others, 1989; Downs and others, 2019
Harrat Bani Abdullah	Ḥarrat Bani Abdallah		South of Harrat Rashid	3 Ma to recent	Camp and Roobol, 1989; Brown and others, 1989
Harrat Turrah	Ḥarrat Turrah	Harrat Turraq		10 Ma to recent	Camp and Roobol, 1989; Brown and others, 1989
Harrat ar Rukhq	Ḥarrat ar Rukhā'	Harrat Ar Rukhq		10–1.7 Ma	Camp and Roobol, 1989; Brown and others, 1989
Harrat al Kishb	Ḥarrat al Kishb			2.4 Ma to recent	Brown and others, 1989; Coleman, 1993; Camp and others, 1992
Harrat Hadan	Ḥarrat Ḥadan			28–15 Ma	Brown and others, 1989; Sebai and others, 1991; Coleman, 1993; Stern and Johnson, 2010; Bosworth and Stockli, 2016

Table 1. Selected Saudi Arabian volcanic fields (harrats), alternate names, radiometric ages, and associated references.—Continued

Harrat name (this study)	Name from Brown and others (1989)	Alternate name	Notes	Age range	References
Harrat Nawāsīf-al Buqūm	Ḥarrat Nawāsīf-al Buqūm	Harrat al Buqūm		5 Ma to recent	Brown and others, 1989
Not used	Ḥarrat ad Damm		Small isolated harrat along Red Sea	7 Ma	Brown and others, 1989
Not used	Ḥarrat Tuffil		Small isolated harrat along Red Sea	2.9–2.8 Ma	Brown and others, 1989
Harrat al Birak	Ḥarrat al Birk	Ḥarrat Hayil, Hubhub al Sheikh		12.4–0.25 Ma	Brown and others, 1989; Coleman, 1993
Harrat as Sirāt	Jabal as Sarāt			30–22.5 Ma	Brown and others, 1989; Camp and Roobol, 1992
Tihāmat ʻAsīr	Tihāmat ʻAsīr			25–21 Ma	Brown and others, 1989
Not used	Ḥarrat Garʻatain				
Not used	Ḥarrat Malaki				

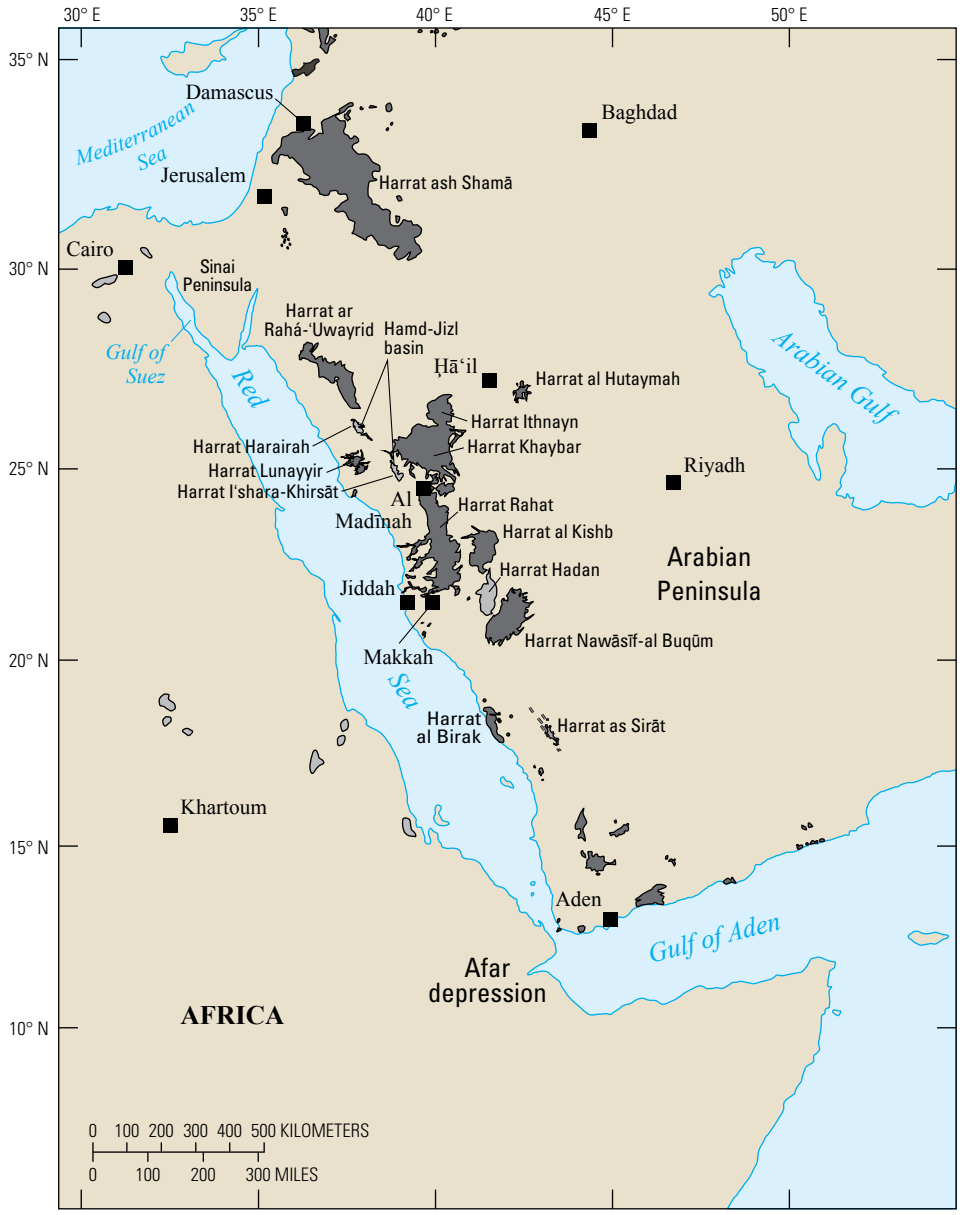

Figure 1. Map of Arabian Peninsula and northeastern Africa. Largest Oligocene (light gray) and younger volcanic fields (dark gray) are shown and labeled. Omitted are young basalts of the Afar depression and older flood basalts of Ethiopia, Sudan, and Yemen, as well as submarine volcanic rocks. Geology from U.S. Geological Survey and Arabian American Oil Company (1963), Coleman and others (1983), Bosworth and others (2005), and Stern and Johnson (2010).

to the Afar depression. Indeed, given its apparent map-view simplicity and textbook example of ruptured continental lithosphere evolving to oceanic spreading, the region and its geodynamics have been studied for decades (Gass, 1970a,b; McKenzie and others, 1970; Buck and others, 1988; Coleman, 1993; Bosworth and others, 2005).

Early studies portrayed the Red Sea as entirely underlain by oceanic crust (McKenzie and others, 1970); however, oceanic drilling, geophysical and bathymetric surveys, and geologic examination of the flanking regions revealed oceanic crust restricted to the southern Red Sea axial trough and the rest of the basin underlain by extended continental crust intruded by Miocene tholeiitic gabbro and basalt dike swarms (Coleman, 1974; Whitmarsh and others, 1974). Research surveys found oceanic crust with mappable magnetic anomalies south of latitude 22° N. and isolated bathymetric deeps to the north, some with volcanic centers, but widely obscured by thick evaporite deposits (Cochran, 2005), some of which have extruded as impressive submarine salt glaciers (Augustin and others, 2014). Geodynamic models indicate axis-normal extension of the Red Sea in the early Miocene, but when oceanic spreading began ~11 Ma in the Gulf of Aden, the Arabia Plate pole of rotation moved to the Gulf of Suez, the Red Sea rifting direction became more northerly, and the magnitude of extension in the northern Red Sea declined (Reilinger and others, 2015). Rifting is nearly aseismic in the northern Red Sea (Mitchell and Stewart, 2018), perhaps owing to the modest extension rate.

Characteristics of Arabian Peninsula Harrats

Late Cenozoic harrats (*harrat* is Arabic for a stony lava field) form a belt from western Yemen northward into Syria and possibly into Turkey, although the tectonic association is uncertain for the northernmost mafic volcanic fields. Western Saudi Arabia hosts some of the largest and most active harrats, where mafic lavas erupted atop a large exposure of Proterozoic basement known as the Arabian Shield (fig. 2), an assemblage of crustal terranes sutured between West (Africa) and East (India) Gondwanaland during the East African orogeny (Stoeser and Camp, 1985; Stern and Johnson, 2010). The shield is exposed in the broad, high-standing, uplifted region of the African-Arabian dome (Almond, 1986b), with the largest harrats either aligned approximately along the crest of the dome and referred to as the Makkah-Madīnah-Nafud, or MMN, line (fig. 2; Camp and others, 1991) or approximately on trend to its north (Harrat ash Shamā, also known as Harrat ash Shāmah and Harrat Shama; table 1). Volcanic rocks of harrats along the MMN line are dominantly weakly alkaline basalts and their differentiation products (hawaiites through trachytes on a silica versus total alkalis plot), whereas the smaller harrats to the west and east include more alkaline rocks, such as basanites through phonolites, and some contain mantle xenoliths that are almost unknown in harrats along the MMN line. Most harrats have elongate shapes (fig. 2) with similarly trending topographically high chains of closely spaced vents, as well as similarly oriented sparse normal faults and fissures, indicative of minimal extensional strain during their growth. A severe earthquake swarm and surface fault rupture in 2009 of the Common Era (C.E.) recorded a shallow dike intrusion along a structure parallel to the Red Sea margin (Pallister and others, 2010). Harrats and their vent alignments have overall northerly trends. Exceptions include northeasterly trends in Harrat Nawāsīf-al Buqūm, the southernmost large harrat, and appreciably west of north in Harrats ar Rahá-al ʻUwayrid and ash Shamā, the northwesternmost and northernmost large harrats.

Lavas marking the onsets of harrat volcanism are exposed only in the deeply eroded harrats whose volcanism waned before the Pleistocene. Lateritic paleosols, lag deposits of coarse, commonly cherty eroded debris, fanglomerates, some containing petrified wood, Proterozoic basement, or (locally) Phanerozoic platform sediments underlie the stratigraphically lowest lavas of most such incised harrats, indicating subaerial emplacement atop a post-Eocene erosion surface (Coleman, 1993). Early lavas from Harrat Hadan (28–10 Ma; Sebai and others, 1991), however, are exposed intercalated with mudstone and limestone (Madden and others, 1980), and chips brought up by exploratory water-well drilling through the northeast end of Harrat Bani Abdullah, a sub-harrat of Harrat Rahat (fig. 3), were interpreted to show that its deepest lava flows are intercalated with Oligocene or possibly older marine sediments (Durozoy, 1972; Brown and others, 1989). These stratigraphic relations indicate that the western Arabian Shield was generally above but close to, and locally below, sea level at the earliest onset of harrat volcanism in the Oligocene.

Harrat Rahat defines the south part of the MMN line, is among the largest of the harrats (about 20,000 square kilometers [km^2]), and comprises four coalescing centers (fig. 3), including Harrat ar Rukhq (8.7–2.5 Ma) in the south to Harrat al Madīnah (also known as Harrat Rashid) (2.5 Ma to recent) in the north (Camp and Roobol, 1989). Harrat Rahat lies in a shallow, north-trending topographic basin centered 20–60 kilometers (km) east of the rugged crest of the Ḥijāz highlands, whose steep western escarpment overlooks the Red Sea coastal plain. In length, Harrat Rahat spans about 310 km from close to Makkah in the south to Al Madīnah in the north. Northern Harrat Rahat, studied in detail by the Saudi Geological Survey (SGS) and the U.S. Geological Survey (USGS), has constructional volcanic relief that, depending on location, rises 300–500 meters (m) above flanking valleys to the west, east, and north that expose Proterozoic basement. Modeling of a gravity survey of northern Harrat Rahat (Langenheim and others, 2019, 2023) yields thicknesses of low-density volcanic rocks and possible underlying low-density sediments similar to the volcanic relief, in places exceeding volcanic relief by no more

than about 200 m, consistent with at most a small graben beneath the most active part of the volcanic field. As noted, Tertiary marine sedimentary rocks underlie some of Harrat Rahat's eruptive loci (Durozoy, 1972), contemporaneous with the deepest lava flows intersected by drilling for water, but because wells were not cored, it is unknown if an appreciable time break or breaks separated initial near-sea-level volcanism from the more extensive younger volcanism that postdated uplift of the Ḥijāz highlands.

Several well-defined sedimentary basins formed subparallel to the Red Sea during continental rifting. These basins accumulated Miocene sediment and grew chiefly by reactivating Proterozoic structures (Camp and Roobol, 1989; Szymanski, 2013; Szymanski and others, 2016). Although no appreciable thickness of Tertiary sediment appears to underlie northern Harrat Rahat, various lines of geologic and geochronologic evidence indicate that the topographic basin that contains it also formed during Miocene tectonism.

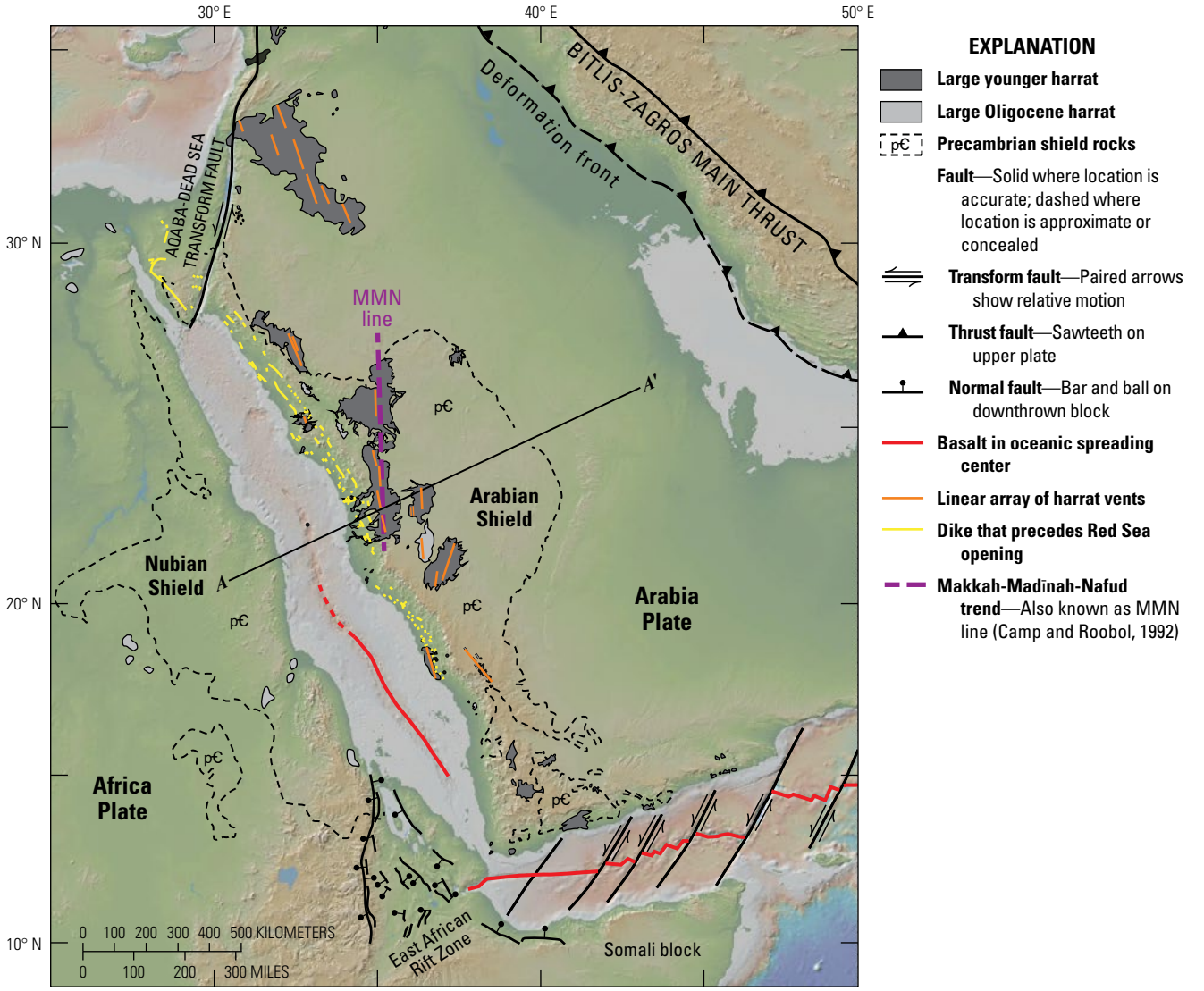

Figure 2. Colored shaded-relief map of Arabian Peninsula and northeastern Africa, showing major tectonic features. Geology from U.S. Geological Survey and Arabian American Oil Company (1963), Coleman and others (1983), Bosworth and others (2005), and Stern and Johnson (2010). Shaded-relief base map and shorelines generated from GeoMapApp (www.geomapapp.org) using global multiresolution topography and bathymetry (Ryan and others, 2009). Line *A*–*A*' shows approximate path of cross section in figure 5.

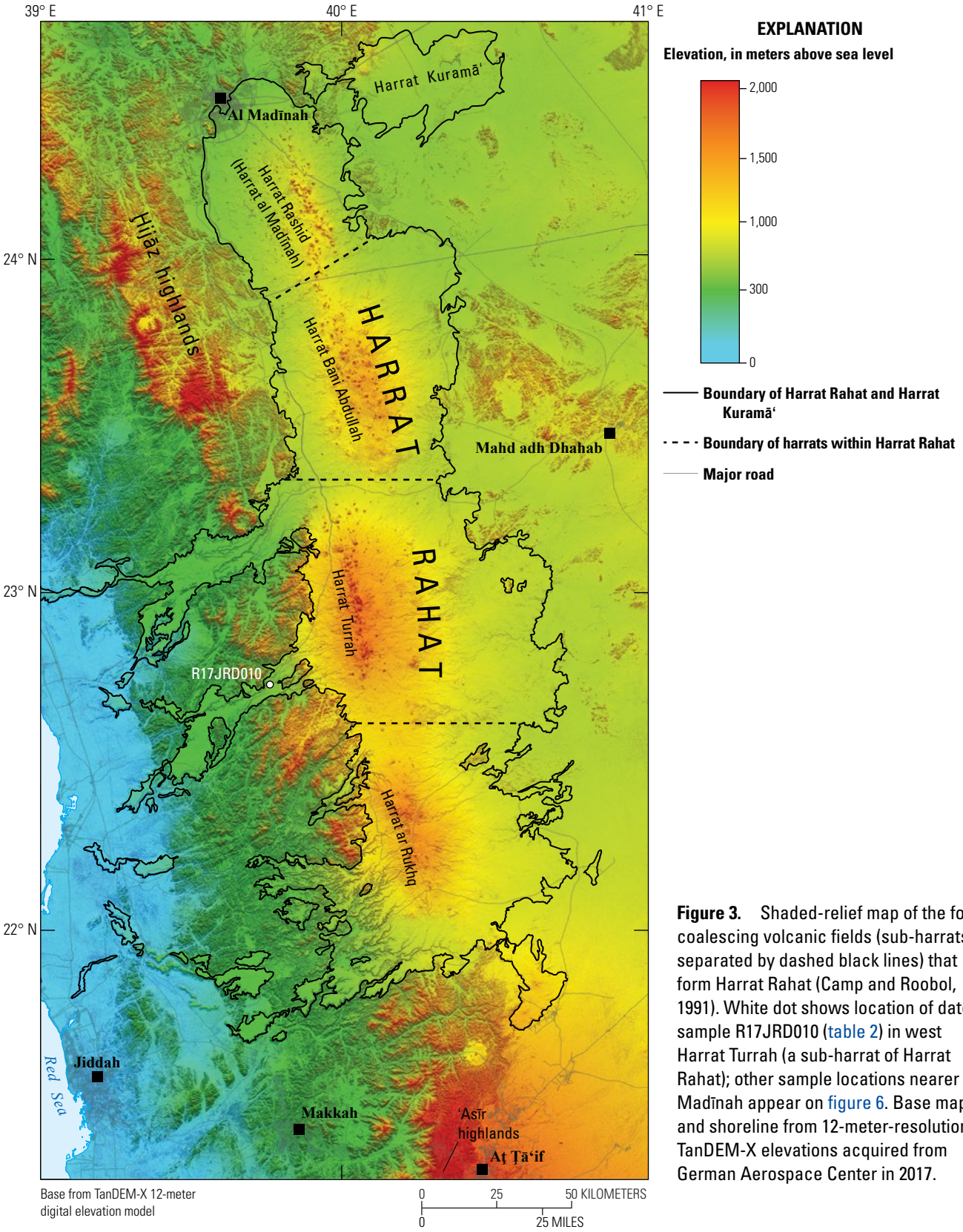

Figure 3. Shaded-relief map of the four coalescing volcanic fields (sub-harrats; separated by dashed black lines) that form Harrat Rahat (Camp and Roobol, 1991). White dot shows location of dated sample R17JRD010 (table 2) in west Harrat Turrah (a sub-harrat of Harrat Rahat); other sample locations nearer Al Madīnah appear on figure 6. Base map and shoreline from 12-meter-resolution TanDEM-X elevations acquired from German Aerospace Center in 2017.

Geologic Setting

The Arabian Shield has a complicated geologic history beginning with the assembly of the Arabian-Nubian Shield, which is composed of mainly Proterozoic juvenile magmatic arcs with coeval deformation, overlain by Paleozoic through lower Cenozoic passive margin sedimentary rocks, then partially exhumed in the early Cenozoic (Bohannon, 1986; Stern and Johnson, 2010). Red Sea rifting began with a dike swarm (fig. 2) that separated the Arabian and Nubian Shields, their split marked by oceanic crust in the southern Red Sea and with rifted continental crust or incipient oceanic spreading in the northern Red Sea. Continental rifting east of the Red Sea formed a series of small grabens and half-grabens whose timing is constrained by thermochronology and coeval volcanism, such as the Hamd-Jizl basin (fig. 1) to the northwest of Harrat Rahat (Szymanski and others, 2016). Topographic basin formation was as old as Oligocene in part, as indicated by the presence of Oligocene sediment beneath lavas in northern Harrat Rahat (Durozoy, 1972). Faulted Pleistocene lavas and aligned fissures within Harrat Rahat indicate that extension continues to the present. Because the volcanic fields are mainly atop the uplifted Arabian dome and are close to its steep western escarpment, it is unclear how much of this modest surficial extension results from far-field plate motions and how much results from flexure of the uplifted part of the Arabia Plate. Geodetic studies are unable to resolve active strain across the Arabian Shield, but analyses of past plate motions require some distributed strain (Reilinger and others, 2015).

Proterozoic Assembly of the Arabian Shield

The Arabian Shield exposes ~770,000 km^2 (Gettings and others, 1986) of deformed plutonic, volcanic, and sedimentary rocks in western Saudi Arabia and Yemen (fig. 2). Similar basement rocks extend 200–300 km underneath Phanerozoic platform sediment to the north and east of the exposed shield (Johnson and Stewart, 1995) and across the Red Sea in Egypt, Sudan, Eritrea, and Ethiopia, where they form the similar-sized Nubian Shield (Johnson and Woldhaimanot, 2003; Nehlig and others, 2002).

Individual terranes exposed on the Arabian Shield (fig. 4) formed as juvenile oceanic magmatic arcs during opening of the Mozambique Ocean owing to breakup of the supercontinent Rodinia at approximately 870 Ma (Johnson and Woldhaimanot, 2003; Stern and Johnson, 2010). The oceanic arcs range in age from 950 to 640 Ma (Stoeser and Camp, 1985), possibly as old as 1,770 Ma (Stacey and Agar, 1985). Some arcs were juxtaposed in amalgamation events between 780–760 Ma, 750–660 Ma, 680–640 Ma, and 650–600 Ma (Fleck and others, 1980; Stoeser and Camp, 1985; Johnson and Woldhaimanot, 2003). Subsequent closing of the Mozambique Ocean led to the Neoproterozoic East African orogeny, accommodated by several orientations of fault systems: (1) the Yanbu-Al Wask and Bir Umq-Thurwah suture zones that trend northeast (Stern and Johnson, 2010) and contain ophiolites and deformed metamorphic rocks (Pallister and others, 1987, 1988) and (2) the Najd Fault System (fig. 4), a 1,200 km long, 300 km wide, en echelon sinistral strike-slip fault system that cuts northwest across the Arabian Shield. Deformation associated with the East African orogeny ended by about 550 Ma (Johnson and Woldhaimanot, 2003). These structures, especially the Najd Fault System, continue to exert controls on Cenozoic faulting patterns, with extensional structures aligned along and coincident with Proterozoic faults.

Two of the oldest arc terranes (fig. 4) in the shield, the Hijaz and Jiddah terranes, underlie Harrat Rahat and other regional structures, including the Hā'il-Rutbah Arch, the MMN line, Red Sea dikes (~25 Ma), and Cenozoic faults that bound extensional basins (Bosworth and others, 2005; Szymanski, 2013; Szymanski and others, 2016). The Hijaz

Figure 4. Map showing the Arabian Shield terranes, faults of the Najd Fault System and pre-Najd-Fault-System accretionary structures (magenta), and suture zones from Stern and Johnson (2010) and Albaroot and others (2016).

terrane in the north includes 870–710 Ma magmatic arcs, hypothesized to have formed in a south-dipping subduction system, and younger extensional basins. The Jiddah terrane underlies southern Harrat Rahat and formed at 870–760 Ma in a northward-migrating southeast-dipping subduction zone (Johnson and Woldhaimanot, 2003). The Hijaz and Jiddah terranes are juxtaposed along the Bir Umq-Thurwah suture zone (Stern and Johnson, 2010).

Paleozoic to Early Cenozoic Passive Margin Sequence

From the early Paleozoic into the early Cenozoic, the Arabian Shield lay along the southern margin of the Paleo-Tethys and Neo-Tethys Oceans, where a thick sequence of dominantly marine passive-margin sediment was deposited (Sharland and others, 2001) around a paleotopographic high to the southwest (Powers and others, 1966). These Arabian Platform sedimentary rocks are exposed north, east, and southeast of Harrat Rahat, but not to its south, suggesting that the western Arabian Shield could have been subaerial during much of the Phanerozoic and never accumulated appreciable sedimentary cover (Powers and others, 1966; Coleman, 1993; Grainger, 2007; Stern and Johnson, 2010).

The Arabian Platform sedimentary section (Powers and others, 1966; Coleman, 1993; Grainger, 2007; Stern and Johnson, 2010) unconformably overlies the Proterozoic Arabian Shield with nonfossiliferous upper Neoproterozoic and, more widely, Cambrian(?) sandstone, overlain by siliciclastic sediments that include Ordovician glacial deposits. Deposition of marine and deltaic siltstones and sandstones occurred through the Devonian and possibly into the Carboniferous as indicated by drillhole observations (Powers and others, 1966). Devonian strata are beveled by a regional unconformity that is overlain by Permian carbonates (glacial deposits in southeastern Saudi Arabia). Triassic terrestrial shales and sandstones are intercalated with marine carbonate, overlain by Jurassic carbonates and evaporites that constitute the major oil reservoir rocks, then overlain by Lower Cretaceous shallow marine and deltaic calcareous sandstones and mudstones. Overlying upper Lower Cretaceous and middle Cretaceous units are distinct from other Mesozoic successions, consisting dominantly of siliciclastic sandstones and subordinate shales of probable marine deposition in the north and subaerial deposition in the south. Marine carbonate deposition then resumed in the Late Cretaceous, with limestone deposited unconformably atop the sandstones. Carbonate deposition persisted into the late Eocene, accompanied by marls and some evaporites. The Samail ophiolite was thrust over oceanic rocks, then emplaced onto the southeastern margin of the pre-rifted Arabia-Nubia Plate from the Campanian to Maastrichtian (Coleman, 1981; Hopson and others, 1981; Searle and Cox, 1999), but, perhaps surprisingly, this event left no distinct signal in the generally carbonate Upper Cretaceous through upper Eocene platform rocks away from the site of emplacement. Oligocene rocks are absent from the platform succession. Instead, upper Eocene detrital-poor carbonates and minor evaporites of regional extent are overlain unconformably by lower Miocene to Pliocene silty and sandy limestones, marls, and some gravels (Powers and others, 1966; Swift and others, 1998), marking widespread uplift, incision, and a final change to clastic sediment transport and deposition.

Regional unconformities or disconformities separate the Devonian from the lower Permian, the lower from the upper Permian, the Triassic from the Jurassic, the Lower Cretaceous from the upper Lower Cretaceous, the upper Lower Cretaceous from the middle Cretaceous, the middle Cretaceous from the Upper Cretaceous, and the Paleogene from the Neogene (Powers and others, 1966). The Paleogene to Neogene unconformity marks the end of widespread passive-margin shelf sedimentation, a change likely coeval with the poorly dated continental collision of the Arabia and Eurasia Plates along the Bitlis-Zagros main thrust (fig. 2), marking closure of the Neo-Tethys Ocean (Koshnaw and others, 2018, and references therein).

Thermochronology of the Hijaz terrane indicates cooling and suggests exhumation of the western Arabian Shield at ~310 Ma, 260–200 Ma, and ~160–120 Ma (Szymanski and others, 2016). The 310 Ma ages correspond to the regional Hercynian orogeny that produced the Devonian to Permian unconformity (Faqira and others, 2009). The 260–200 Ma ages appear related to an eastern Mediterranean rifting event (Guiraud and Bosworth, 1999) and may encompass both the lower Permian to upper Permian and Triassic to Jurassic unconformities. The ~160–120 Ma ages are linked to the breakup of Pangea (Szymanski and others, 2016) and correspond to the period of Cretaceous clastic sedimentation with its bounding and internal unconformities (Powers and others, 1966). Facies changes in middle Cretaceous rocks across the east trending Central Arabian Arch (lat ~24° N.) and the north trending Hā'il-Rutbah Arch (long ~42°30′ E.) indicate that those structures had relief and were possibly developing at that time (Powers and others, 1966).

Cenozoic Uplift and Exhumation of the Arabian Shield

The uplift and exhumation histories of the Arabian and Nubian Shields are known mainly from indirect evidence. The shields' broadest exposures and greatest relief flank the central Red Sea, not the Afar depression, and the shields lack overlying Afar plume flood basalts, so evidence to support uplift driven directly by the Afar mantle plume is lacking. Except for the Cambrian(?) and middle Cretaceous episodes of siliciclastic sandstone deposition and the Ordovician glacial deposits, the Arabian Platform sedimentary section is dominated by carbonates of nearshore to shelf deposition with periods of evaporite deposition through the late Eocene. Those parts of what is now the Arabia Plate were widely but shallowly submerged, with no substantive sources of terrigenous siliciclastic sediments as might have been shed

from an extensively emergent, nearby, high-relief shield. Nevertheless, the near absence of platform rocks atop the exposed Arabian Shield, contrasting with their accumulation to multi-kilometer thicknesses to the north, east, and southeast, prompt many authors (for example, Powers and others, 1966; Almond, 1986b) to interpret that the area now between the Red Sea and the central Arabian Shield was emergent, or only briefly and thinly buried during most of the Phanerozoic. Such interpretation is supported by low-temperature thermochronology, which yields Paleozoic and Mesozoic ages of shield exhumation (Bohannon and others, 1989; Szymanski and others, 2016). The west-central shield may have been a low-relief, low-elevation emergent landmass along the shore of the Tethys Oceans during the Phanerozoic, but the central shield now stands approximately 1 km above sea level, requiring substantial, widespread uplift following platform sedimentation.

The platform sedimentary rocks wrap around and dip away from the Arabian Shield, changing strike across the Central Arabia and Hā‘il-Rutbah Arches that define the shield's eastern and north-central exposures. Facies changes across the arches developed in the Cretaceous (Powers and others, 1966), indicating that those structures largely developed after most of the platform sediments were deposited. Pre-Cenozoic relief and exposure of the shield is shown by Cretaceous(?) fluvial sandstones that directly overlie the Proterozoic shield on the northeastern and southern margins of Harrat Hadan, due east of Makkah (Brown and others, 1963; Madden and others, 1980). In the central and eastern Arabian Peninsula, Arabian Gulf, and into Ar Rub‘ al Khālī, lower Miocene and younger clastic sedimentary rocks were deposited unconformably atop the platform sequence (Powers and others, 1966; Swift and others, 1998). Therefore, widespread Cenozoic uplift of the Arabian Shield is bracketed between deposition of the upper Eocene marine carbonates and before or during deposition of lower Miocene silty limestones, marls, and gravels.

In detail, the latest Mesozoic to early Cenozoic was marked by a marine transgression from the north, encroaching on and burying the uppermost Lower Cretaceous and middle Cretaceous sandstones and lower platform rocks (Powers and others, 1966; Madden and others, 1979; Coleman, 1993; Grainger, 2007). Cretaceous rocks are exposed along the north-trending Hā‘il-Rutbah Arch, so this structure has been interpreted as having had positive relief and formed an eastern margin to a shallow early Cenozoic seaway that eventually crossed the presently exposed shield. Sedimentary successions along the western shield also record the latest Mesozoic to early Cenozoic transgression. Paleocene mudstone and shale containing estuarine vertebrate fauna, succeeded by dolomitic limestone, unconformably overlie both the Proterozoic shield and Cretaceous(?) fluvial sandstones beneath Harrat Hadan (Madden and others, 1979; Bohannon and others, 1989). The Upper Cretaceous to lower Eocene Usfan Formation northeast of Jiddah also records a transgressive succession from fluvial sandstones to shallow marine carbonates (Abou Ouf and Gheith, 1998). A lack of strong extensional faulting and resulting offsets of the Paleozoic to lower Cenozoic passive-margin sequence along the proposed seaway is inconsistent, however, with substantial or widespread plate extension accompanying transgression into the early Cenozoic. Instead, the exposed shield and flanking platform rocks were probably never much above sea level immediately before, and were little deformed during, the late Mesozoic to early Cenozoic transgression. The succeeding final uplift of the shield appears to have been en masse, at least away from the Red Sea, recorded by the outward dips of the platform strata and by the upper Eocene to lower Miocene unconformity (Powers and others, 1966; Swift and others, 1998), with its change from shelf-carbonate to clastic sedimentation, as well as by a lack of accommodating Miocene faults within the shield. Coleman (1993) interpreted a northward spread of Cenozoic uplift but cites no supporting evidence.

Oligocene to Miocene Inception of Red Sea Spreading and Related Volcanism

The Red Sea and Gulf of Aden are the most visible components of the African-Arabian rift system (Bosworth, 2015), which extends from the East African Rift Zone in the south to the Gulf of Suez and Dead Sea in the north and eastward to the Indian Ocean (or Arabian Sea). The Red Sea south of latitude 22° N. and the Gulf of Aden have documented oceanic seafloor spreading, complete with striped magnetic anomalies (Phillips, 1970; Cochran, 1983). Red Sea bathymetric deeps to 1,500 m, some with imaged and sampled volcanic centers, are present between latitudes 22° and 24° N. (Bosworth and others, 2005; Augustin and others, 2014). In contrast, the Gulf of Suez and the northern Red Sea and its flanks are characterized by continental rifting (Steckler, 1985; Cochran, 2005; Bosworth, 2015). Thick evaporite sediments obscure the axial trough in the northern Red Sea, so it is unclear where sea-floor spreading ends.

Almond (1986a), Bohannon and others (1989), Coleman (1993), Bosworth (2015), and Szymanski and others (2016) discussed timing and magnitude of extension within and adjacent to the Red Sea from study of sedimentary basins, volcanic successions, geochronology, and thermochronology. Volcanic constraints are reviewed by Bosworth and Stockli (2016). A sequence of Oligocene to Miocene extensional and volcanic events are now recognized and well dated (Bosworth, 2015).

- *Continental flood basalt volcanism (31–30 Ma).*— Voluminous basaltic volcanism, followed shortly by rhyolitic eruptions, blanketed large parts of Ethiopia, southeast Sudan, and western Yemen, associated with the Afar plume (Gass, 1970a; Zumbo and others, 1995; Baker and others, 1996). These continental flood basalts, covering more than 600,000 km^2, have a cumulative volume estimated to be greater than 350,000 (Mohr, 1983) to more than 1 million

cubic kilometers (km^3) (Courtillot and others, 1999). Early published ages from Afar and the Ethiopian plateau ranged from 34 to 15 Ma (Mohr and Zanettin, 1988), a span later narrowed to 31–27 Ma (Hoffman and others, 1997); however, sanidine from plateau-capping sections yields 30–27 Ma (Hoffman and others, 1997) and 30.1±0.1 to 30.2±0.1 Ma (Rochette and others, 1998), so the flood basalt episode was likely brief. Timing constraints are similar in the South Sudan Red Sea Hills and Yemen with most of the flood basalt erupted 31–30 Ma and continuing sporadically until about 26.5 Ma and evolving locally into rhyolites (compiled by Bosworth and Stockli, 2016). Stratigraphic relations, such as interlayering of lava flows with shallow marine sedimentary rocks, indicate some eruptions were close to sea level (Coleman, 1993), but other evidence indicates at least localized uplift commenced perhaps 10 million years before flood-basalt volcanism (Sembroni and others, 2016; Faccenna and others, 2019). Most uplift associated with the Afar plume followed flood-basalt volcanism (Sembroni and others, 2016; Faccenna and others, 2019) and is apparent today as the high-elevation regions surrounding the Afar depression, including across the Red Sea in western Yemen and southwesternmost Saudi Arabia.

- *The older harrats (30–22 Ma).*—Scattered 30–22 Ma basaltic eruptive centers span a north-northwest-trending lineament from the Yemen-Saudi Arabia border into Syria (fig. 2; Pallister, 1987; Stern and Johnson, 2010). These include Harrat as Sirāt (30–25 Ma; Camp and Roobol, 1992) in southern Saudi Arabia, older parts of Harrat Hadan (28–15 Ma; Sebai and others, 1991) east of Makkah, and older parts of Harrat ash Shamā (27–22 Ma; Ilani and others, 2001) in northern Saudi Arabia, Jordan, and Syria (Bosworth and Stockli, 2016).

- *Rifting, dikes, and inception of rift-shoulder uplift (24–20 Ma).*—Syn-rift basin deposits are locally exposed adjacent to the Red Sea and northward along the Gulf of Suez, containing laterally discontinuous beds of sandstone and conglomerate, typically with lava flows, pyroclastic material, or detrital volcanic clasts (Sellawood and Netherwood, 1984) providing evidence of syn-extensional volcanism. Fossils indicate the syn-rift sequence is upper Oligocene (Chattian, 27.5–23.0 Ma) in a small rift basin beside the Eritrean Red Sea (Hughes and others, 1991; Bosworth, 2015), and early Miocene (Aquitanian, 23.0–20.4 Ma) in the Gulf of Suez (Bosworth and others, 2005). Regionally the transition to syn-rift sedimentation is at the base of the Burdigalian, about 20.4 Ma (Bosworth, 2015). An extensive suite of northwest-striking tholeiitic basalt dikes intruded along the length of the Red Sea margin from Yemen to the Sinai Peninsula and northern Egypt (fig. 2) between 24 and 20 Ma (Bosworth and Stockli, 2016). In the Gulf of Suez, these dikes intrude basal syn-rift sedimentary successions (Sellawood and Netherwood, 1984). Voluminous lava flows in the subsurface of the Cairo basin are coeval with the regional dikes. Paleomagnetic evidence indicates those flows were erupted in two brief periods (Lotfy and others, 1995), both between 24 and 21 Ma (Bosworth and others, 2015). Low-temperature thermochronology using fission track and U-Th/He methods indicates exhumation of the Arabian Shield along the Saudi Arabian margin of the Red Sea began locally at 24–23 Ma and regionally by 22–20 Ma (Szymanski and others, 2016). Marine syn-tectonic sediments were deposited during this interval (24-20 Ma) from Eritrea (Hughes and others, 1991) to the Gulf of Suez (Bosworth and others, 2005; Bosworth, 2015), indicating that the rift axis lay below sea level by the Oligocene to Miocene transition. Thermochronology from crystalline rocks collected on the Sinai Peninsula (Kohn and Eyal, 1981), eastern Egypt along the Gulf of Suez (Omar and others, 1989), and southern Arabia along the Red Sea (Bohannon and others, 1989) indicates the rift-shoulder uplift began 24–20 Ma (Bosworth, 2015). Farther south, thermochronology results indicate exhumation as young as 17–16 Ma (Menzies and others, 1997; Ghebreab and others, 2002) and 10 Ma (Abbate and others, 2002), but modeling indicates the bulk of cooling occurred from 24 to 20 Ma (Bosworth, 2015). The agreement between stratigraphic constraints on rifting deposits and low-temperature thermochronology offers strong evidence that exhumation of the Arabian Shield was driven by uplift, as opposed to simple erosion.

- *Rift flank uplift (16–11 Ma).*—Lavas radiometrically dated at 16–15 Ma from Harrat I‘shara-Khirsāt (Szymanski, 2013) are interbedded with clastic sedimentary rocks in the Hamd–Jizl half-graben (fig. 1) near latitude 25° N. (Coleman, 1993), 150–170 km east of the Red Sea shoreline, indicating some extension distributed within the rift shoulder, not just at the Red Sea. Harrat I‘shara-Khirsāt volcanic rocks are not discernably tilted or faulted, but the base of the volcanic section lies 200–600 m above the valley to the east, explained most readily by subsequent offset across an unrecognized extensional fault system. Coeval thermochronology results, including apatite U-Th/He from along the central Arabian rift flank (lat 21–29° N., Szymanski and others, 2016) and apatite fission tracks with long track-length distributions from the southern rift flank (lat 17–21° N.; Bohannon and others, 1989), indicate rapid cooling at about 15–14 Ma, inferred to be related to rapid uplift of the Arabian Shield (Camp and

Roobol, 1989; Szymanski and others, 2016). Lavas that now cap mesas just west and southwest of Al Madīnah are 14–12 Ma, coeval with syn-tectonic lavas erupted in Harrat I'shara-Khirsāt, described below.

- *Young harrat volcanism (10 Ma–present).*—Alkali basalts to trachytes (locally to phonolites) erupted to build volcanic fields subparallel to the Red Sea from 10 Ma to present, most with north to north-northwest vent alignments. The majority of Saudi Arabian harrats are 100–350 km east or northeast of the coast, measured perpendicular to the Red Sea shoreline, although some vents are as distant as 570 km (Harrat al Hutaymah) or along the coast (Harrat al Birak). The most voluminous of the Saudi Arabian centers (Harrats Rahat, Khaybar, and Ithnayn), located along the MMN line, lie above a north-trending belt with anomalously slow (hot) upper mantle seismic velocities (fig. 5) identified in tomographic images (Chang and others, 2011). As noted, volcanic rocks of the harrats to the east and west of the MMN line include more alkaline compositions and contain some or many mantle xenoliths, collectively indicating lower extents of partial melting and faster ascents from mantle depths than for magmas that fuel the harrats along the MMN line (Camp and others, 1991).

New $^{40}Ar/^{39}Ar$ Constraints on Structures in and Adjacent to Harrat Rahat

The four coalesced volcanic centers that make up Harrat Rahat grew in a broad, shallow, north-trending valley system 20–60 km east of the crest of the Ḥijāz highlands (fig. 3). Oligocene marine sediments recovered from below Harrat Rahat (Durozoy, 1972) raise the possibility that the structural basin began to form as early as the onset of rift flank uplift. Here we present five new $^{40}Ar/^{39}Ar$ ages (table 2) from lava flows that date and bracket events prior to the northern Harrat Rahat volcanism radiometrically dated by Stelten and others (2023). Several of these new ages provide more precise constraints on results compiled and reported by Camp and Roobol (1991).

Harrat Kuramā' and Harrat I'shara-Khirsāt are lesser studied and poorly dated, older alkalic volcanic centers located 30–100 km east and 60–120 km north-northwest of Al Madīnah, respectively (Camp and Roobol, 1991; Szymanski, 2013). Small, flat-lying remnants of basalt and basanite lava flows that unconformably cap several hills of Proterozoic intrusive and metavolcanic rocks 5–10 km west and southwest of Al Madīnah's center (fig. 6) are similar in composition to Harrat Kuramā' (50 km east of Al Madīnah) and Harrat I'shara-Khirsāt (70 km northwest of Al Madīnah).

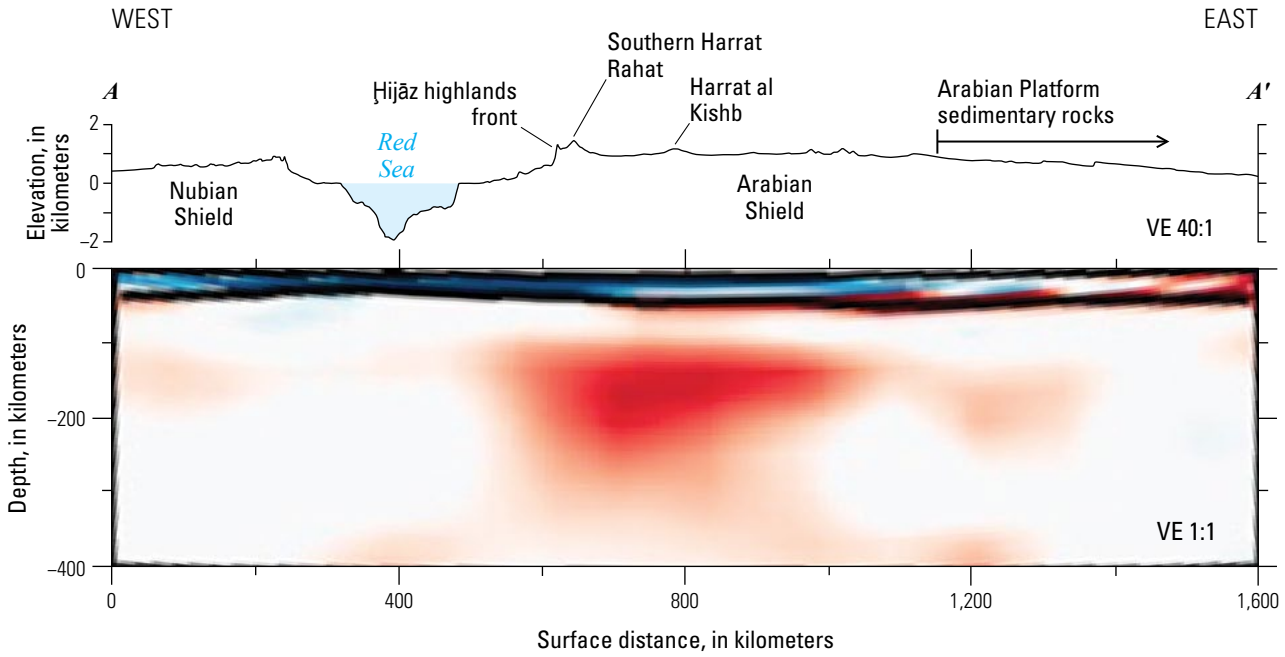

Figure 5. Geophysical cross section *A*–*A*' perpendicular to Red Sea near latitude 23° N., across parts of the Nubian and Arabian Shields (see fig. 2 for approximate location). Shown in varying hues are perturbations of shear-wave upper-mantle velocity relative to reference velocity. Red shows anomalously slow velocities (300 meters per second [m/s] decrease for darkest red color); blue shows anomalously fast velocities (300 m/s increase for darkest blue color) (Chang and others, 2011). Topographic profile with 40:1 vertical exaggeration (VE) created using GeoMapApp (www.geomapapp.org) and global multiresolution topography and bathymetry (Ryan and others, 2009).

Table 2. New $^{40}Ar/^{39}Ar$ ages of volcanic rocks collected adjacent to Harrat Rahat.

[See appendix 1 for methods and raw results. Samples are groundmass feldspar concentrations. Irradiated at U.S. Geological Survey TRIGA reactor using 9.7946-Ma Bodie Hills sanidine as a neutron flux monitor (Fleck and others, 2019). Preferred ages in bold typeface. Latitude and longitude in decimal degrees using World Geodetic System of 1984 (WGS84) projection. Ma, mega-annum; T, temperature; °C, degree Celsius; %, percent; MSWD, mean square of weighted deviates]

Sample	Latitude	Longitude	Material	$^{40}Ar/^{39}Ar$ weighted mean plateau age			$^{40}Ar/^{39}Ar$ isotope correlation (isochron) age				$^{40}Ar/^{39}Ar$ total gas
				Age ±1σ (Ma)	^{39}Ar, in % [T range, in °C]	MSWD	Age ±1σ (Ma)	^{39}Ar, in % [T range, in °C]	MSWD	$^{40}Ar/^{36}Ar_i$ ±2σ	Age ±1σ (Ma)
R17TS219	24.57002	39.75374	Basalt groundmass	**2.15±0.01**[a]	75 [700–1,175]	0.38	2.14±0.03	75 [700–1,175]	0.4	300.2±6.8	2.18±0.1
R17JRD010	22.73887	39.75858	Basalt groundmass	**2.94±0.02**[a]	100 [550–1,250]	1.87	2.93±0.03	100 [550–1,250]	1.4	299.6±4.5	2.98±0.02
R17AC158	24.47576	39.47621	Basanite groundmass	**12.33±0.04**[a]	38 [525–625]	2.2	12.40±0.08	38 [525–625]	2.11	294.6±8.5	12.36±0.02
R17AC157	24.40438	39.46413	Basanite groundmass	13.41±0.06	52 [600–800]	9.33	**12.95±0.08**[a]	52 [600–800]	0.41	330.3±12.9	12.98±0.02
R17AC155	24.37382	39.57411	Basalt groundmass	**13.56±0.03**[a]	39 [700–900]	0.2	13.58±0.05	39 [700–900]	0.23	296.0±16.4	13.38±0.03

[a]Preferred age.

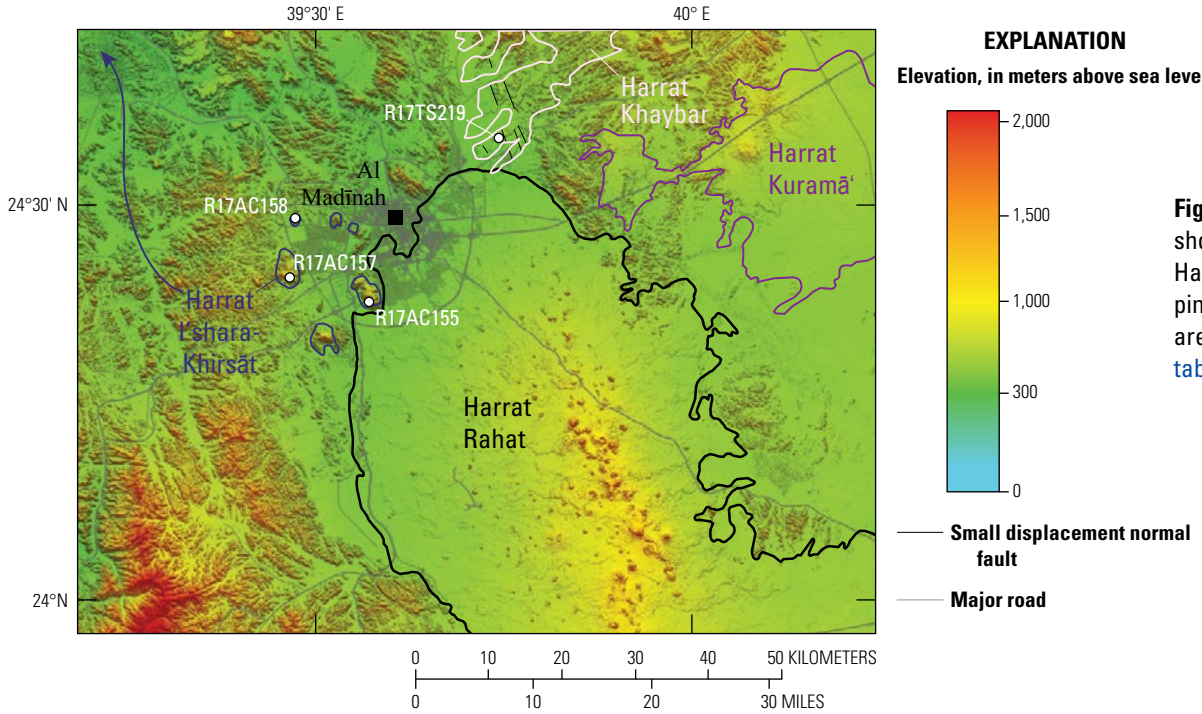

Figure 6. Expanded view of shaded-relief map (fig. 3) showing northern Harrat Rahat and parts of neighboring Harrat I'shara-Khirsāt (blue outline), Harrat Khaybar (light pink outline), and Harrat Kuramā' (purple outline). White dots are geochronology sample locations near Al Madīnah. See table 2 for Ar-Ar geochronologic data for these samples.

The basal contacts of these lavas are 200–350 m higher in elevation than the adjacent valley that underlies Harrat Rahat (fig. 7). Lavas range from 13.6 to 12.3 Ma (samples R17AC155–158, table 2), coeval with syn-tectonic basalts from Harrat I'shara-Khirsāt that flowed into the Hamd-Jizl basin (Szymanski, 2013). Mesa-capping lavas are untilted, but tectonic interpretations are limited by a lack of Miocene sediments exposed with the lavas (to confirm stratal dip) or of recognized faults between lava plateaus and the adjacent topographic basin that underlies Harrat Rahat. These units were radiometrically dated by Pellaton (1981) at 11.1±0.8 and 7.7±0.7 Ma and were included on the Camp and Roobol (1991) geologic map. These new 14–12 Ma $^{40}Ar/^{39}Ar$ ages match Harrat I'shara-Khirsāt ages reported by Szymanski (2013).

Lavas from the vigorous growth of Harrat Rahat clearly postdated rift-shoulder uplift, demonstrated by voluminous, deeply incised flows that drape the Ḥijāz highland's west-facing escarpment and that reach or cross the Red Sea coastal plain. Northwest-trending faults mapped by Camp and Roobol (1991) that cut Harrat Rahat lavas do not appear (on modern satellite imagery) to offset lavas more than 5 m. Volcanism following uplift is borne out by argon geochronology on Harrat Rahat lavas; Camp and Roobol (1991) summarized and evaluated the few K-Ar ages then available for Harrat Rahat, concluding that the oldest determination of which they were confident was 8.7 Ma but that Harrat Rahat's volcanism may have commenced at about 10 Ma. A stratigraphically low, incised, escarpment-draping lava whose $^{40}Ar/^{39}Ar$ age is 2.9 Ma, determined in this study (sample R17JRD010; fig. 3; table 2), is consistent with K-Ar ages (13 to 2 Ma; Camp and Roobol, 1991) for the voluminous lavas that descended drainages west of Harrat Rahat. Interstratification of deeply buried lava flows with Oligocene marine sediments in drill holes that penetrate Harrat Rahat (Durozoy, 1972) can be reconciled with post-uplift volcanism if the deep subsurface flows correlate with older periods of volcanism, such as the mesa-capping lavas near Al Madīnah and those of Harrat I'shara-Khirsāt, or even older, rather than being early products of Harrat Rahat itself. This proposed age of onset is similar to thermochronology results indicating uplift of the rift flank Ḥijāz-'Asīr highlands at 16–14 Ma (Bohannon and others, 1989; Szymanski and others, 2016).

Extension continues to the present, as vent alignments, fissures, and faults are oriented strongly north-northwesterly in the active parts of Harrat Rahat. Linear concentrations of vents that define the high-standing eruptive axes of Harrat Rahat imply abundant parallel feeder dikes at depth, and the ridge-like constructional volcanic relief of Harrat Rahat's four component sub-harrats further indicates that dikes repeatedly injected in about the same places and with the same trends, consistent with a dominant extensional fault beneath each sub-harrat. Nevertheless, few faults have been discovered cutting lava flows within the volcanic field. A network of small-displacement normal faults offsets a basalt flow (2.15 Ma; sample R17TS219; table 2; fig. 6) northeast of Al Madīnah; this and nearby flows probably erupted from southern Harrat Khaybar, but possibly from Harrat Kuramā', rather than from Harrat Rahat. A north-striking normal fault with ~10 m of offset also cuts a ~250-thousand-year-old (ka) lava flow (Downs and others, 2019; Robinson and Downs, 2023) within northern Harrat Rahat. A chain of cinder cones aligned 25° west of north (N. 25° W.) erupted at about 13 ka

Figure 7. Photograph of one of several hills in the western suburbs of Al Madīnah capped by Miocene basalt (this one undated) unconformably atop eroded Proterozoic metavolcanic and metaintrusive rocks. Arrows indicate near-horizontal unconformity about 175 meters above the valley floor. Photograph by A. Calvert, U.S. Geological Survey.

in what is now the southwest suburb of Al Madīnah (Stelten and others, 2023). Fissures in the field trend N. 20° W. to N. 30° W. and cut lavas as young as 151 ka (Downs and others, 2019; Robinson and Downs, 2023); however, scrutiny of alluvial fans and sabkha flats on 1-m and 4-m digital elevation models that span northern Harrat Rahat and its surroundings show no fault offsets, indicating that extension from the late Pleistocene to the present is accommodated mainly by dike intrusion and does not extend appreciably beyond the areas of active volcanism. Surficial extensional features of the harrats, including their orientations, probably result from a combination of far-field plate-scale motions and flexure of the uplifted Arabian dome and rift shoulder but with unknown relative contributions.

Oligocene to Present Plate Tectonic Model

Reilinger and others (2015) presented a regional tectonic model for the Nubia, Arabia, and Eurasia Plate interactions from the Oligocene to the present. (1) Prior to Red Sea and Gulf of Aden rifting, the Africa Plate moved north or northeast toward Eurasia, likely pulled by subduction of the Tethys Ocean slab as it was consumed beneath the Eurasia Plate. The Paleocene was a period of slow Arabia-Eurasia convergence, possibly even stopping, resuming at about 30 millimeters per year (mm/yr) from the Eocene into the Oligocene, then declining as the continents collided along the Bitlis-Zagros suture (McQuarrie and others, 2003; Agard and others, 2011). (2) During the late Oligocene to early Miocene the Afar plume weakened the Africa Plate underneath present-day Ethiopia, Yemen, and Somalia, allowing Arabia to fracture from Africa along the future Red Sea and Gulf of Aden lineaments (Reilinger and others, 2015). The Red Sea does not follow Proterozoic structural boundaries, so it is probably oriented approximately orthogonal to the then direction of slab pull. More northerly volcanic lineaments in western Saudi Arabia and Jordan may result from lithospheric weakening owing to underplating, as indicated by 30-Ma and younger mantle-derived harrat magmatism. (3) East- to northeast-directed approximately axis-normal extension of the Red Sea, as indicated by piercing points along the Red Sea coast, continued until about 11 Ma. The Dead Sea Transform fault disengaged the Sinai Peninsula from the Arabia Plate around 14–12 Ma (Bosworth and McClay, 2001; Bosworth, 2015). (4) At 11±2 Ma, sea-floor spreading volcanism in the Gulf of Aden signaled separation of the Arabia Plate from the Somali block; separation of the plates greatly decreased resistance to slab pull and allowed the Arabia Plate to move in a more northerly direction. Extension directions across the Red Sea shifted from rift-normal (northeast to southwest) to oblique (north-northeast to south-southwest) (Bosworth, 2015). The Arabia Plate's new (and current) pole of rotation is near the Gulf of Suez, causing significant variation in Red Sea spreading rates with respect to Nubia from 17.2 mm/yr in Yemen to only 6.8 mm/yr near the Sinai Peninsula (Reilinger and others, 2015).

Red Sea Pure-Shear versus Simple-Shear Tectonic Models

The Red Sea was recognized as a continental rift long ago (Wegener, 1929), even before and as plate tectonic theory was developed, along with recognition of the Gulf of Aden and East African Rift Zone (Baker, 1970; McKenzie and others, 1970; Burke and Dewey, 1973; Coleman, 1974). Early workers hypothesized (Baker, 1970), then confirmed (Whitmarsh and others, 1974), the presence of oceanic crust in the southern Red Sea. Subsequent work showed that the Gulf of Suez—the northern end of the rift—is underlain by continental crust, and the central and northern Red Sea is crust of transitional character. Early models to explain Red Sea evolution (Mohr, 1970; McKenzie and others, 1970; Burke and Dewey, 1973) described the rifting as essentially symmetrical (pure shear), with oceanic spreading developing following a normal-faulted rift valley. Elevated topography is inferred to result from the Afar plume (Gass, 1970a; Ebinger and Sleep, 1998; Chang and others, 2011; Sembroni and others, 2016), Red Sea rifting (Bohannon and others, 1989; Szymanski and others, 2016), or probably both, depending on location.

Differences in topography and abundance of volcanic rocks between the Arabian and African sides of the Red Sea led Wernicke (1985), Voggenreiter and others (1988), and Tesfaye and Ghebreab (2013) to propose that an east-dipping, lithosphere-scale, simple-shear detachment fault system created the rift, with the Egypt-Sudan escarpment being the western surface exposure of the master fault (upper crustal breakaway; fig. 12 of Wernicke [1985]), and the high topography of the Arabian Shield as the uplifted headwall rocks above a detachment fault, there 50–80 km deep. The high topography of the Arabian Shield would result from buoyant asthenosphere that replaced denser lithosphere displaced westward in the footwall (topographic culmination; fig. 12 of Wernicke [1985]). This simple-shear interpretation does not explain why a single fault system would transect the entire crust and mantle lithosphere, nor does it address fault mechanics or the pore-fluid pressures required to favor a 10–30° dipping normal fault instead of a steeply dipping structure (Anderson, 1951); however, it does offer an explanation for asymmetry, including disparate rift shoulder elevations and abundances of volcanic fields. Other workers envision formation of initially high-angle faults that rotated to lower angles, which were then cut by new sets of high-angle faults (for example, Perry and Schamel, 1990). Heat flow modeling favors pure-shear extension models, discussed in the following section.

Discussion and Summary

Rifting of the Arabian Peninsula from Africa offers a young, simple-appearing example of continental lithospheric breakup (McKenzie and others, 1970; Burke and Dewey, 1973). These early studies hypothesized the formation of rift-rift-rift triple junctions in uplifted crust supported by mantle plumes, with the Ethiopian plateau and the now Afar depression above the plume and the Gulf of Aden, East African Rift Zone, and Red Sea as rifts at ~120° angles. Decades of study of the Red Sea and its flanks support much of this model but expose complications that can help clarify the processes driving rifting and volcanism. In particular, the mix of continental and oceanic spreading in the basins, the abundance of Miocene and younger volcanic centers on the Arabian Peninsula (but not on the west side of the Red Sea), trends of volcanic vents within these centers oblique to Red Sea structural trends, and geophysical evidence of thin lithosphere beneath parts of the western Arabia Plate suggest that regional tectonics and magmatism are not driven only by Red Sea extension.

Magnitude, Orientations, and Timing of Extension in Western Arabia

Volcanic features of the harrats provide evidence for extension of the shallow parts of the Arabia Plate. High-standing vent axes of Harrat Rahat's constituent sub-harrats trend from N. 13° W. to N. 26° W., and the topographic and vent axis of Harrat Khaybar, the large harrat to the north that lies on the MMN line, trends about N. 4° W. (fig. 2). Extension perpendicular to these would be N. 77° E. to N. 64° E., and N. 86° E., respectively, whereas Global Positioning System (GPS) measurements (Reilinger and others, 2015) show current separation of Arabia from Nubia in the direction of N. 40° E. to N. 50° E. in the vicinities of southern Harrat Rahat and the northern ʻAsīr highlands, and N. 30° E. to N. 40° E. in northwestern Saudi Arabia approaching the Sinai Peninsula. Disparities between extension directions indicated by volcanic features and motion of Arabia from Nubia are even greater for Harrat Nawāsīf-al Buqūm (lat 21° N., long 42° E.) where vent axes trend N. 20° E. to N. 30° E., within 20°–30° of the plate separation direction. Directions of dike opening indicated by harrat vent alignments are not, therefore, simple expressions of plate separation encroaching into the continent. GPS measurements reveal no strain across western Saudi Arabia (Reilinger and others, 2015) so active extension is either too slow to detect over the short span of observations, or it is episodic, perhaps related to volcanic activity as at Harrat Lunayyir in 2009 C.E. (Pallister and others, 2010); in any event, upper crustal extension is minor.

Factors that would complicate relations between directions of plate separation and near-surface extension include preexisting basement structures, arching and flexure of the uplifted Arabian dome, and related to this, the pronounced shallowing of the base of the mantle lithosphere localized beneath harrats along the MMN line. Proterozoic lithosphere of the tectonically inactive and amagmatic Nubian Shield is 120–180 km thick (Artemieva and Mooney, 2001), and lithosphere beneath the Arabian Platform may reach as much as 160 km depth (Hansen and others, 2007), whereas the lithosphere-asthenosphere boundary is in the range of only 60–90 km deep in a narrow belt generally beneath the MMN line (Chang and others, 2011; Yao and others, 2017). Stern and Johnson (2010) proposed that some of the sub-shield thinning was ancient, caused by delamination of dense arc roots following continental assembly. This delamination caused initial uplift and exhumation of the intrusive and metamorphic Arabian and Nubian Shield rocks, with Proterozoic and Paleozoic apatite fission track thermochronology (Bohannon and others, 1989), providing a minimum age on Arabian Shield exhumation. Alternatively, the shield may have been exhumed simply by erosion of overthickened crust. Whether ancient loss of arc roots or erosion of overthickened crust accounts for the shield's initial exhumation, its current height at ~1 km above sea level was caused by some process in the Cenozoic. Arabian Shield crust is neither commensurately thinned nor strongly extensionally faulted where the lithosphere is thin, and ongoing geodetic displacement rates show negligible intraplate extension, so it appears that approximately half of the lithosphere beneath the belt of largest and most active harrats has been lost from below by some process. Chang and others (2011) interpreted that thin lithosphere and shear wave splitting parallel to the MMN line (Gashawbeza and others, 2004; Hansen and others, 2006) result from Afar plume material spreading preferentially beneath the MMN line; however, Stern and Johnson (2010) cautioned that those splitting orientations are similar to Proterozoic arc trends and could be fossil features from continental assembly. Additionally, geochemical and isotopic studies conclude that Harrat Rahat volcanic rocks are related more to midocean ridge basalts (MORB) than to Afar plume magmas (Sisson and others, 2023; Salters and others, 2023). A subordinate plume component is present in the magmas' sources, but asthenosphere beneath and fueling the harrats on the MMN line is dominated by common depleted upper mantle that yields alkalic magmas owing to lower degrees of partial melting and deeper melt separation than produce tholeiitic MORB. Those authors propose that lithospheric mantle beneath the MMN line may be foundering through a magmatic feedback process, with plume-contaminated ambient asthenosphere upwelling and partially melting in response. Seismicity in the mantle lithosphere beneath the edge of the MMN line is consistent with rapid and recent loss of the deeper lithosphere; otherwise, conduction of heat from the asthenosphere would have prevented brittle failure (Blanchette and others, 2018).

Mechanism of Extension

Heat flow measurements indicate that rocks flooring the Red Sea basin are unusually hot (Girdler and Evans, 1977; Martinez and Cochran, 1988) and require a crustal thinning zone that was initially widening and broad as extension progressed, then abruptly narrowed at ~5 Ma to its presently active width of ~20 km (Buck and others 1988; Martinez and Cochran, 1989; Makris and others, 1991). Heat flow models do not allow for lithospheric-scale detachment geometry as proposed by Wernicke (1985) and Tesfaye and Ghebreab (2013), rather they require very hot Neogene mantle upwelling, otherwise the shallow heat flow would have had time to equilibrate (Buck and others, 1988).

Why the lithosphere thinned beneath the MMN line is difficult to understand, especially with little continental extension above. Paleogeographic reconstruction by Sisson and others (2023) showed that prior to Red Sea opening, the south end of the belt of Arabia Plate thinned lithosphere was adjacent to the northern end of what is now the Afar depression at the north end of the East African Rift Zone. Those authors speculated that a continuous arch in the base of the pre-rifting Arabia-Nubia Plate underlay and connected the now northern East African Rift Zone with the harrats that now form the MMN line and that buoyant Afar plume materials preferentially channeled along that arch system, as proposed for other parts of northern Africa (Ebinger and Sleep, 1988). A magmatic feedback mechanism may then have initiated, similar to that proposed for the Siberian Traps (Elkins-Tanton, 2005), wherein partial melts intruded the deep lithospheric arch and solidified as dense eclogites, causing foundering of the injected and densified region. Ambient upper mantle asthenosphere then upwelled into the vacating region, undergoing further decompression partial melting, thereby removing mantle lithosphere from below. If correct, the considerable thinning of the deep lithosphere and development of the Arabia Plate harrats may have only a loose connection to the particulars of Cenozoic extension.

Perhaps the strongest evidence for a clear link between harrat volcanism and tectonism is the onset of voluminous late Cenozoic basaltic eruptions at about 10 Ma, shortly following uplift of the Ḥijāz-ʻAsīr highlands, initiation of Aqaba-Dead Sea Transform faulting, separation of Arabia from the Somali block, commencement of Gulf of Aden seafloor spreading, and the change in Arabia Plate motion. Older harrats, mainly closer to the Red Sea (Harrats ar Rahá-al ʻUwayrid, Iʻshar-Khirsāt, and Harairah), but some at greater distance (Harrats as Sirāt and Hadan), diminished or ceased erupting entirely, with volcanism shifting mainly to the MMN-line centers and to younger parts of Harrat ash Shamā. Tholeiitic seafloor volcanism in the Gulf of Aden, and later in the southern Red Sea, indicates that depleted asthenosphere had upwelled to shallow depths beneath the spreading axes, having transected most or all thick subcontinental lithosphere. Although upwelling is commonly thought of as a passive process driven by thinning of the overlying plate, an active mantle circulation component can participate. The asthenosphere is commonly interpreted as having an adiabatic-isentropic pressure-temperature gradient because it is thought to be convecting (Turcotte and Schubert, 2014). Regions of focused upwelling would heat and erode the deep lithosphere, and once upwelling convection reached sufficiently shallow depths, partial melting would commence with magmatic diking, which further heats and weakens the overlying lithosphere. Liberation of the Arabia Plate from Africa and the Somali block, uplift of the Red Sea rift shoulder and the Arabian dome, breakthrough of the Aqaba-Dead Sea Transform fault system, and the flaring up of harrat volcanism on the MMN line, all by approximately 10 Ma, may be diverse consequences of the mantle lithosphere having thinned more beneath volcanically active areas and less in those areas that are uplifted but sparsely volcanic or nonvolcanic. In this interpretation, the Afar plume may have initiated lithospheric thinning, in part by spreading beneath the lithosphere and in part by enhancing thermal convection of the ambient asthenosphere. If the Arabian Shield was already underlain by thinner mantle lithosphere (Stern and Johnson, 2010), that region would tend to capture and focus enhanced upwelling. Once focused convection was established, however, the process may have acted largely on its own or with reduced fueling from the Afar plume stem.

Whether through focused convection in the uppermost asthenosphere, with or without a magmatic feedback mechanism (Sisson and others, 2023), or from a finger of the hot Afar plume that spread beneath the Arabia Plate, the mantle lithosphere was eroded substantially beneath the MMN line, uplifting and, as with other regions, weakening the lithosphere. Normal faulting is not prominent on the Arabian Shield, but if continued to completion, westernmost Arabia may rift along the belt of thin lithosphere (Chang and others, 2011), eventually separating a narrow sliver of continental crust preserved between the Red Sea on the west and a new seaway on the east running along the present MMN line to perhaps Harrat ash Shamā, and from there connecting to the Aqaba-Dead Sea Transform system. Many analogous crustal fragments are preserved as fault-bounded slivers in ancient terranes.

Acknowledgments

We thank Dave Sherrod, John Pallister, and Jeff Doebrich for thoughtful reviews. Juliet Ryan-Davis and Jamal Shawali helped collect lavas dated in this study. The Saudi Geological Survey provided funding, transportation, and logistical support.

References Cited

Abbate, E., Balestrieri, M.L., and Bigazzi, G., 2002, Morphostructural development of the Eritrean rift flank (southern Red Sea) inferred from apatite fission track analysis: Journal of Geophysical Research, v. 107, no. B11, p. 2319.

Abou Ouf, M.A., and Gheith, A.M., 1998, Sedimentary evolution of early rift troughs on the central Red Sea margin, Jeddah, Saudi Arabia, *in* Pursner, B.H., and Bosense, D.W., eds., Sedimentation and tectonics in rift basins—Red Sea–Gulf of Aden: London, Chapman and Hall, p. 135–145.

Agard, P., Omrani, J., Jolivet, L., Whitechurch, H., Vrielynck, B., Spakman, W., Monié, P., Meyer, B., and Wortel, R., 2011, Zagros orogeny—A subduction-dominated process: Geological Magazine, v. 148, nos. 5–6, p. 692–725.

Albaroot, M., Ahmad, A.H.M., Al-Areeq, N., and Sultan, M., 2016, Tectonostratigraphy of Yemen and geological evolution—A new prospective: International Journal of New Technology and Research, v. 2, no. 2, p. 19–33.

Almond, D.C., 1986a, The relation of Mesozoic-Cainozoic volcanism to tectonics in the Afro-Arabian dome: Journal of Volcanology and Geothermal Research, v. 28, p. 225–246.

Almond, D.C., 1986b, Geological evolution of the Afro-Arabian dome: Tectonophysics, v. 131, p. 301–332.

Anderson, E.M., 1951, The dynamics of faulting (rev. ed.): Edinburgh, Oliver and Boyd, 206 p.

Artemieva, I.M., and Mooney, W.D., 2001, Thermal thickness and evolution of Precambrian lithosphere—A global study: Journal of Geophysical Research, v. 106, p. 16387–16414.

Augustin, N., Devey, C.W., van der Zwan, F.M., Feldens, P., Tominaga, M., Bantan, R.A., and Kwasnitschka, T., 2014, The rifting to spreading transition in the Red Sea: Earth and Planetary Science Letters, v. 395, p. 217–230.

Baker, B.H., 1970, The structural pattern of the Afro-Arabian rift system in relation to plate tectonics: Philosophical Transaction of the Royal Society of London, Series A, Mathematical and Physical Sciences, v. 267, p. 383–391.

Baker, J.A., Thirlwall, M.F., and Menzies, M.A., 1996, A brief Oligocene period of flood volcanism in Yemen—Implications for the duration and rate of continental flood volcanism at the Afro-Arabian triple junction: Earth and Planetary Science Letters, v. 138, nos. 1–4, p. 39–55.

Blanchette, A.R., Klemperer, S.L., Mooney, W.D., and Zahran, H.M., 2018, Two-stage Red Sea rifting inferred from mantle earthquakes in Neoproterozoic lithosphere: Earth and Planetary Science Letters, v. 497, p. 92–101.

Bohannon, R.G., 1986, Tectonic configuration of the western Arabian continental margin, southern Red Sea: Tectonics, v. 5, no. 4, p. 477–499.

Bohannon, R.G., Naeser, C.W., Schmidt, D.L., and Zimmerman, R.A., 1989, The timing of uplift, volcanism, and rifting peripheral to the Red Sea—A case for passive rifting?: Journal of Geophysical Research, v. 94, no. B2, p. 1683–1701.

Bosworth, W., 2015, Geological evolution of the Red Sea—Historical background, review and synthesis, *in* Rasul, N.M., and Stewart, I.C.F., eds., The Red Sea: Berlin, Springer-Verlag, p. 45–78.

Bosworth, W., Huchon, P., and McClay, K., 2005, The Red Sea and Gulf of Aden Basins, *in* Catuneanu, O., Guiraud, R., Eriksson, P., Thomas, B., Shone, R., and Key, R., eds., Phanerozoic evolution of Africa: Journal of African Earth Sciences, v. 43, p. 334–378.

Bosworth, W., and McClay, K., 2001, Structural and stratigraphic evolution of the Gulf of Suez rift, Egypt—A synthesis, *in* Ziegler, P.A., Cavazza, W., Robertson, A.H.F., and Crasquin-Soleau, S., eds., Peri-Tethys Memoir 6—Peri-Tethyan rift/wrench basins and passive margins: Memoires du Museum National d'Histoire Naturelle de Paris, v. 186, p. 567–606.

Bosworth, W., and Stockli, D., 2016, Early magmatism in the greater Red Sea rift—Timing and significance: Canadian Journal of Earth Science, v. 53, p. 1158–1176.

Bosworth, W., Stockli, D.F., and Helgeson, D.E., 2015, Integrated outcrop, 3D seismic, and geochronologic interpretation of Red Sea dike-related deformation in the Western Desert, Egypt—The role of the 23 Ma Cairo "mini-plume": Journal of African Earth Sciences, v. 109, p. 107–119.

Brown, G.F., Jackson, R.O., Bogue, R.G., and MacLean, W.H., 1963, Geologic map of the southern Hijaz quadrangle, Kingdom of Saudi Arabia: U.S. Geological Survey Miscellaneous Geologic Investigations Map I-210A, scale 1:500,000.

Brown, G.F., Schmidt, D.L., and Huffman, A.C., Jr., 1989, Geology of the Arabian Peninsula—Shield area of western Saudi Arabia: U.S. Geological Survey Professional Paper 560-A, p. A1–A188.

Buck, R., Martinez, F., Steckler, M.S., and Cochran, J.R., 1988, Thermal consequences of lithospheric extension—Pure and simple: Tectonics, v. 7, p. 213–234.

Burke, K., and Dewey, J.F., 1973, Plume-generated triple junctions—Key indicators in applying plate tectonics to old rocks: Journal of Geology, v. 81, p. 406–433.

Camp, V.E., and Roobol, M.J., 1989, The Arabian continental alkali basalt province; Part I—Evolution of Harrat Rahat, Kingdom of Saudi Arabia: Geological Society of America Bulletin, v. 101, p. 71–95.

Camp, V.E., and Roobol, M.J., 1991, Geologic map of the Cenozoic lava field of Harrat Rahat, Kingdom of Saudi Arabia: Ministry of Petroleum and Mineral Resources, GM–123, scale 1:250,000, pamphlet 37 p.

Camp, V.E., and Roobol, M.J., 1992, Upwelling asthenosphere beneath western Arabia and its regional implications: Journal of Geophysical Research, v. 97, p. 15255–15271.

Camp, V.E., Roobol, M.J., and Hooper, P.R., 1991, The Arabian continental alkali basalt province; Part II—Evolution of Harrats Khaybar, Ithnayn, and Kura, Kingdom of Saudi Arabia: Geological Society of America Bulletin, v. 103, p. 363–391.

Camp, V.E., Roobol, M.J., and Hooper, P.R., 1992, The Arabian continental alkali basalt province; Part III—Evolution of Harrat Kishb, Kingdom of Saudi Arabia: Geological Society of America Bulletin, v. 104, p. 379–396.

Chang, S.J., Merino, M., Van der Lee, S., Stein, S., and Stein, C.A., 2011, Mantle flow beneath Arabia offset from the opening Red Sea: Geophysical Research Letters, v. 38, no. 4, article L04301, 5 p.

Cochran, J.R., 1983, A model for the development of the Red Sea: American Association of Petroleum Geologists Bulletin, v. 67, p. 41–69.

Cochran, J.R., 2005, Northern Red Sea—Nucleation of an oceanic spreading center within a continental rift: Geochemistry, Geophysics, Geosystems, v. 6, article Q03006, 34 p.

Coleman, R.G., 1974, Geologic background of the Red Sea, *in* Whitmarsh R.B., Weser, O.E., and Ross, D.A., eds., Initial reports of the deep sea drilling project: Government Printing Office, Washington, v. 23, p. 813–819.

Coleman, R.G., 1981, Tectonic setting for ophiolite obduction in Oman: Journal of Geophysical Research, v. 86, no. B4, p. 2497–2508.

Coleman, R.G., 1993, Geologic evolution of the Red Sea: Oxford Monographs on Geology and Geophysics, v. 24, 186 p.

Coleman, R.G., Gregory, R.T., and Brown, G.F., 1983, Cenozoic volcanic rocks of Saudi Arabia: U.S. Geological Survey Open-File Report 83-788, 1 plate, 82 p.

Courtillot, V., Jaupart, C., Manighetti, I., Tapponnier, P., and Besse, J., 1999, On causal links between flood basalts and continental breakup: Earth and Planetary Science Letters, v. 166, p. 177–195.

Downs, D.T., Robinson, J.E., Stelten, M.E., Champion, D.E., Dietterich, H.R., Sisson, T.W., Zahran, H., Hassan, K., and Shawali, J., 2019, Geologic map of the northern Harrat Rahat volcanic field, Kingdom of Saudi Arabia: U.S. Geological Survey Scientific Investigations Map 3428 [also released as Saudi Geological Survey Special Report SGS–SP–2019–2], 65 p., 4 sheets, scales 1:75,000, 1:25,000, https://doi.org/10.3133/sim3428.

Durozoy, G., 1972, Hydrogeologic des basalts du Harrat Rahat (Royaume d' Arabic Scoudite): France, Bureau de Recherches Geologiques et Minieres Bulletin, ser. 2, sect. 3, no. 2, p. 37–50.

Ebinger, C.J., and Sleep, N.H., 1988, Cenozoic magmatism throughout east Africa resulting from a single plume: Nature, v. 395, p. 788–791.

Elkins-Tanton, L.T., 2005, Continental magmatism caused by lithospheric delamination, *in* Foulger, G.R., Natland, J.H., Presnall, D.C., and Anderson, D.L., eds., Plates, plumes, and paradigms: Geological Society of America Special Paper 388, p. 449–461.

Faccenna, C., Glišović, P., Forte, A., Becker, T., Garzanti, E., Sembroni, A., and Gvirtzman, Z., 2019, Role of dynamic topography in sustaining the Nile River over 30 million years: Nature Geoscience, v. 12, p. 1012–1017.

Faqira, M., Rademakers, M., and Afifi, A., 2009, New insights into the Hercynian Orogeny, and their implications for the Paleozoic hydrocarbon system in the Arabian Plate: GeoArabia, v. 14, no. 3, p. 199–228.

Fleck, R.J., Calvert, A.T., Coble, M.A., Wooden, J.L., Hodges, K., Hayden, L.A., van Soest, M.C., du Bray, E.A., and John, D.A., 2019, Characterization of the rhyolite of Bodie Hills and $^{40}Ar/^{39}Ar$ intercalibration of Ar mineral standards: Chemical Geology, v. 525, p. 282–302.

Fleck, R.J., Greenwood, W.R., Hadley, D.G., Anderson, R.E. and Schmidt, D.L., 1980, Rubidium-strontium geochronology and plate-tectonic evolution of the southern part of the Arabian Shield: U.S. Geological Survey Professional Paper 1131, 38 p.

Gashawbeza, E.M., Klemperer, S.L., Nyblade, A.A., Walker, K.T., and Keranen, K.M., 2004, Shear-wave splitting in Ethiopia: Geophysical Research Letters, v. 31, article L18602, 4 p.

Gass, I.G., 1970a, Tectonic and magmatic evolution of the Afro-Arabian dome, *in* Clifford, T.E., and Gass, I.G., eds., African magmatism and tectonics: Edinburgh, Oliver and Boyd, p. 285–300.

Gass, I.G., 1970b, The evolution of volcanism in the junction area of the Red Sea, Gulf of Aden and Ethiopian rifts: Philosophical Transactions Royal Society of London, Series A, Mathematical, Physical, and Engineering Sciences, v. 267, p. 369–381.

Gettings, M.E., Blank, H.R., Mooney, W.D., and Healy, J.H., 1986, Crustal structure of southwestern Saudi Arabia: Journal of Geophysical Research, v. 91, p. 6491–6512.

Ghebreab, W., Carter, A., Hurford, A.J., and Talbot, C.J., 2002, Constraints for timing of extensional tectonics in the western margin of the Red Sea in Eritrea: Earth and Planetary Science Letters, v. 200, no. 1, p. 107–119.

Girdler, R.W., and Evans, T.R., 1977, Red Sea heat flow: Geophysical Journal of the Royal Astronomical Society, v. 51, p. 245–251.

Grainger, D., 2007, The geologic evolution of Saudi Arabia—A voyage through space and time: Jiddah, Saudi Arabia, Saudi Geological Survey, v. 1, 264 p.

Guiraud, R., and Bosworth, W., 1999, Phanerozoic geodynamic evolution of northeastern Africa and the northwestern Arabian platform: Tectonophysics, v. 315, p. 73–108.

Hansen, S.E., Rodgers, A.J., Schwartz, S.Y., and Al-Amri, A.M.S., 2007, Imaging ruptured lithosphere beneath the Red Sea and Arabian Peninsula: Earth and Planetary Science Letters, v. 259, p. 256–265.

Hansen, S.E., Schwartz, S., Al-Amri, A., and Rodgers, A., 2006, Combined plate motion and density-driven flow in the asthenosphere beneath Saudi Arabia—Evidence from shear-wave splitting and seismic anisotropy: Geology, v. 34, no. 10, p. 869–872.

Hoffman, C., Courtillot, V., Féraud, G., Rochette, P., Yirgu, G., Ketefo, E., and Pik, R., 1997, Timing of the Ethiopian flood basalt event and implications for plume birth and global change: Nature, v. 389, p. 838–841.

Hopson, C.A., Coleman, R.G., Gregory, R.T., Pallister, J.S., and Bailey, E.H., 1981, Geologic section through the Samail Ophiolite and associated rocks along a Muscat-Ibra transect, southeastern Oman Mountains: Journal of Geophysical Research, v. 86, no. B4, p. 2527–2544.

Hughes, G.W., Varol, O., and Beydoun, Z.R., 1991, Evidence for middle Oligocene rifting of the Gulf of Aden and for late Oligocene rifting of the southern Red Sea: Marine and Petroleum Geology, v. 8, p. 354–358.

Ilani, S., Harlavan, Y., Tarawneh, K., Rabba, I., Weinberger, R., and Ibrahhim, K., 2001, New K-Ar ages of basalts from the Harrat Ash Shaam volcanic field in Jordan—Implications for the span and duration of the upper-mantle upwelling beneath the western Arabian Plate: Geology, v. 29. p. 171–174.

Johnson, P.R., and Stewart, I.C.F., 1995, Magnetically inferred basement structure in central Saudi Arabia: Tectonophysics, v. 245, nos. 1–2, p. 37–52.

Johnson, P.R., and Woldhaimanot, B., 2003, Development of the Arabian-Nubian Shield—Perspectives on accretion and deformation in the East African Orogen and the assembly of Gondwana, *in*, Yoshida, M., Windley, B.F., and Dasgupta, S., eds., Proterozoic East Gondwana—Supercontinent assembly and breakup: Geological Society of London Special Publication, v. 206, p. 289–325.

Kohn, B.P., and Eyal, M., 1981, History of uplift of the crystalline basement of Sinai and its relation to opening of the Red Sea as revealed by fission track dating of apatites: Earth and Planetary Science Letters, v. 52, no. 1, p. 219–239.

Koshnaw, R.I., Stockli, D.F., and Schlunegger, F., 2018, Timing of the Arabia-Eurasia continental collision—Evidence from detrital zircon U-Pb geochronology of the Red Bed Series strata of the northwest Zagros hinterland, Kurdistan region of Iraq: Geology, v. 47, no. 1, p. 47–50.

Langenheim, V.E., Ritzinger, B.T., Zahran, H., Shareef, A., Al-dahri, M., 2019, Crustal structure of the northern Harrat Rahat volcanic field (Saudi Arabia) from gravity and aeromagnetic data: Tectonophysics, v. 750, p. 9–21.

Langenheim, V.E., Ritzinger, B.T., Zahran, H.M., Shareef, A., and Al-Dhahry, M.K., 2023, Depth to basement and crustal structure of the northern Harrat Rahat volcanic field, Kingdom of Saudi Arabia, from gravity and aeromagnetic data, chap. K *of* Sisson, T.W., Calvert, A.T., and Mooney, W.D., eds., Active volcanism on the Arabian Shield—Geology, volcanology, and geophysics of northern Harrat Rahat and vicinity, Kingdom of Saudi Arabia: U.S. Geological Survey Professional Paper 1862 [also released as Saudi Geological Survey Special Report SGS–SP–2021–1], 18 p., https://doi.org/10.3133/pp1862K.

Lotfy, H.I., Van der Voo, R., Hall, C.M., Kamel, O.A., and Abdel Aal, A.Y., 1995, Palaeomagnetism of early Miocene basaltic eruptions in the areas east and west of Cairo: Journal of African Earth Sciences, v. 21, p. 407–419.

Madden, C.T., Naqvi, I.M., Whitmore, F.E., Jr., Schmidt, D.L., Langston, W., and Wood, R.C., 1980, Paleocene vertebrates from coastal deposits in the Harrat Hadan area, At Taif region, Kingdom of Saudi Arabia: U.S. Geological Survey Open File Report 80-227, 29 p.

Makris, J., Tsironidis, J., and Richter, H., 1991, Heatflow density distribution in the Red Sea: Tectonophysics, v. 198, p. 383–393.

Martínez, F., and Cochran, J.R., 1988, Structure and tectonics of the northern Red Sea: Catching a continental margin between rifting and drifting: Tectonophysics, v. 150, p. 1–32.

Martínez, F., and Cochran, J.R., 1989, Geothermal measurements in the northern Red Sea—Implications for lithospheric thermal structure and mode of extension during continental rifting: Journal of Geophysical Research, v. 94, no. B9, p. 12239–12265.

McKenzie, D.P., Davies, D., and Molnar, P., 1970, Plate tectonics of the Red Sea and East Africa: Nature, v. 226, p. 243–248.

McQuarrie, N., Stock, J.M., Verdel, C., and Wernicke, B.P., 2003, Cenozoic evolution of Neotethys and implications for the causes of plate motions: Geophysical Research Letters, v. 30, 4 p., https://doi.org/10.1029/2003GL017992.

Menzies, M., Gallagher, K., Yelland, A., and Hurford, A.J., 1997, Volcanic and nonvolcanic rifted margins of the Red Sea and Gulf of Aden—Crustal cooling and margin evolution in Yemen: Geochimica et Cosmochimica Acta, v. 61, no. 12, p. 2511–2527.

Mitchell, N.C., and Stewart, I.C.F., 2018, The modest seismicity of the northern Red Sea rift: Geophysical Journal International, v. 214, p. 1507–1523.

Mohr, P., 1970, The Afar triple junction and sea-floor spreading: Journal of Geophysical Research, v. 75, p. 7340–7352.

Mohr, P., 1983, Ethiopian flood basalt province: Nature, v. 303, p. 577–584.

Mohr, P., and Zanettin, B., 1988, The Ethiopian flood basalt province, *in* Macdougall, J.D., ed., Continental flood basalts: Dordrecht, Kluwer Academic Publishers, p. 63–110.

Nehlig, P., Genna, A., and Asirfane, F., 2002, A review of the Pan-African evolution of the Arabian Shield: GeoArabia, v. 7, p. 103–124.

Omar, G.I., Steckler, M.S., Buck, W.R., and Kohn, B.P., 1989, Fission-track analysis of basement apatites at the western margin of the Gulf of Suez rift, Egypt—Evidence for synchroneity of uplift and subsidence: Earth and Planetary Science Letters, v. 94, no. 3, p. 316–328.

Pallister, J.S., 1984, Reconnaissance geology of the Harrat Hutaymah quadrangle, sheet 26/42A, Kingdom of Saudi Arabia: U.S. Geological Survey Open-File Report 85-125, 2 plates, 77 p.

Pallister, J.S., 1987, Magmatic history of Red Sea rifting—Perspective from the central Saudi Arabian coastal plain: Geological Society of America Bulletin, v. 98, p. 400–417.

Pallister, J.S., McCausland, W., Jónsson, S., Lu, Z., Zahran, H.M., El Hadidy, S., Aburukbah, A., Stewart, I.C.F., Lundgren, P.R., White, R.A., and Moufti, M.R.H., 2010, Broad accommodation of rift-related extension recorded by dyke intrusion in Saudi Arabia: Nature Geoscience, v. 3, p. 705–712, https://doi.org/10.1038/ngeo966.

Pallister, J.S., Stacey, J.S., Fischer, L.B. and Premo, W.R., 1987, Arabian Shield ophiolites and Late Proterozoic microplate accretion: Geology, v. 15, p. 320–323.

Pallister, J.S., Stacey, J.S., Fischer, L.B., and Premo, W.R., 1988, Precambrian ophiolites of Arabia—Geologic settings, U-Pb geochronology, Pb-isotope characteristics, and implications for continental accretion: Precambrian Research, v. 38, p. 1–54.

Pellaton, C., 1981, Geologic map of the Al Madinah quadrangle, sheet 24D, Kingdom of Saudi Arabia: Saudi Arabian Deputy Ministry for Mineral Resources Geoscience Map GM–52, scale 1:250,000, 19 p.

Perry, S.K., and Schamel, S., 1990, The role of low-angle normal faulting and isostatic response in the evolution of the Suez Rift, Egypt: Tectonophysics, v. 174, p. 159–173.

Phillips, J.D., 1970, Magnetic anomalies in the Red Sea: Philosophical Transactions of the Royal Society London, Series A, Mathematical and Physical Sciences, v. 267, p. 205–217.

Powers, R.W., Ramirez, L.F., Redmond, C.D., and Elberg, E.L., Jr., 1966, Geology of the Arabian Peninsula—Sedimentary geology of Saudi Arabia: U.S. Geological Survey Professional Paper 560–D, 147 p.

Reilinger, R., McClusky, S., and ArRajehi, A., 2015, Geodetic constraints on the geodynamic evolution of the Red Sea, *in* Rasul, N.M.A., and Stewart, I.C.F., eds., The Red Sea: Springer Earth System Sciences, 638 p.

Robinson, J.E., and Downs, D.T., 2023, Overview of the Cenozoic geology of the northern Harrat Rahat volcanic field, Kingdom of Saudi Arabia, chap. R *of* Sisson, T.W., Calvert, A.T., and Mooney, W.D., eds., Active volcanism on the Arabian Shield—Geology, volcanology, and geophysics of northern Harrat Rahat and vicinity, Kingdom of Saudi Arabia: U.S. Geological Survey Professional Paper 1862 [also released as Saudi Geological Survey Special Report SGS–SP–2021–1], 20 p., scale 1:100,000, https://doi.org/10.3133/pp1862R.

Rochette, P., Tamrat, E., Féraud, G., Pik, R., Courtillot, V., and Kefeto, E., 1998, Magnetostratigraphy and timing of the Oligocene Ethiopian traps: Earth and Planetary Science Letters, v. 164, p. 497–510.

Ryan, W.B.F., Carbotte, S.M., Coplan, J.O., O'Hara, S., Melkonian, A., Arko, R., Weissel, R.A., Ferrini, V., Goodwillie, A., Nitsche, F., Bonczkowski, J., and Zemsky, R., 2009, Global multi-resolution topography synthesis: Geochemistry, Geophysics, Geosystems, v. 10, article Q03014, 9 p., https://doi.org/10.1029/2008GC002332.

Salters, V.J.M., Sachi-Kocher, A., Downs, D.T., Stelten, M.E., and Sisson, T.W., 2023, Isotopic and geochemical evidence for the source of volcanism at Harrat Rahat, Kingdom of Saudi Arabia, chap. J *of* Sisson, T.W., Calvert, A.T., and Mooney, W.D., eds., Active volcanism on the Arabian Shield—Geology, volcanology, and geophysics of northern Harrat Rahat and vicinity, Kingdom of Saudi Arabia: U.S. Geological Survey Professional Paper 1862 [also released as Saudi Geological Survey Special Report SGS–SP–2021–1], 30 p., https://doi.org/10.3133/pp1862J.

Searle, M., and Cox, J., 1999, Tectonic setting, origin, and obduction of the Oman ophiolite: Geological Society of America Bulletin, v. 111, p. 104–122.

Sebai, A., Zumbo, V., Féraud, G., Bertrand, H., Hassain, A.G., Giannérini, G., and Campredon, R., 1991, $^{40}Ar/^{39}Ar$ dating of alkaline and tholeiitic magmatism of Saudi Arabia related to the early Red Sea rifting: Earth and Planetary Science Letters, v. 104, p. 473–487.

Sellawood, B.W., and Netherwood, R.E., 1984, Facies evolution in the Gulf of Suez area—Sedimentation history as an indicator of rift initiation and development: Modern Geology, v. 9, p. 43–69.

Sembroni, A., Faccenna, C., Becker, T.W., Molin, P., and Abebe, B., 2016, Long-term, deep-mantle support of the Ethiopia-Yemen Plateau: Tectonics, v. 35, p. 469–488.

Sharland, P.R., Archer, R., Casey, D.M., Davies, R.B., Hall, S.H., Heward, A.P., Horbury, A.D., and Simmons, M.D., 2001, Arabian Plate sequence stratigraphy: GeoArabia Special Publication 2, 371 p.

Sisson, T.W., Downs, D.T., Calvert, A.T., Dietterich, H.R., Mahood, G.A., Salters, V.J.M., Stelten, M.E., and Shawali, J., 2023, Mantle origin and crustal differentiation of basalts and hawaiites of northern Harrat Rahat, Kingdom of Saudi Arabia, chap. I *of* Sisson, T.W., Calvert, A.T., and Mooney, W.D., eds., Active volcanism on the Arabian Shield—Geology, volcanology, and geophysics of northern Harrat Rahat and vicinity, Kingdom of Saudi Arabia: U.S. Geological Survey Professional Paper 1862 [also released as Saudi Geological Survey Special Report SGS–SP–2021–1], 42 p., https://doi.org/10.3133/pp1862I.

Stacey, J.S., and Agar, R.A, 1985, U-Pb isotopic evidence for the accretion of a continental microplate in the Zalm region of the Saudi Arabian Shield: Journal of the Geological Society of London, v. 142, p. 1189–1203.

Steckler, M.S., 1985, Uplift and extension at the Gulf of Suez—Indications of induced mantle convection: Nature, v. 317, p. 135–139.

Stelten, M.E., Downs, D.T., Champion, D.E., Dietterich, H.R., Calvert, A.T., Sisson, T.W., Mahood, G.A., and Zahran, H.M., 2023, Eruptive history of northern Harrat Rahat—Volume, timing, and composition of volcanism over the past 1.2 million years, chap. D *of* Sisson, T.W., Calvert, A.T., and Mooney, W.D., eds., Active volcanism on the Arabian Shield—Geology, volcanology, and geophysics of northern Harrat Rahat and vicinity, Kingdom of Saudi Arabia: U.S. Geological Survey Professional Paper 1862 [also released as Saudi Geological Survey Special Report SGS–SP–2021–1], 46 p., https://doi.org/10.3133/pp1862D.

Stern, R.J., and Johnson, P., 2010, Continental lithosphere of the Arabian Plate—A geologic, petrologic, and geophysical synthesis: Earth-Science Reviews, v. 101, p. 29–67.

Stoeser, D.B., and Camp, V.E., 1985, Pan-African microplate accretion of the Arabian Shield: Geological Society of America Bulletin, v. 96, no. 7, p. 817–826.

Swift, S.A., Uchupi, E., and Ross, D.A., 1998, Late Cenozoic geology of the central Persian (Arabian) Gulf from industry well data and seismic profiles: Woods Hole Oceanographic Institution Technical Memorandum WHOI–01–98, 75 p.

Szymanski, E., 2013, Timing, kinematics, and spatial distribution of Miocene extension in the central Arabian margin of the Red Sea rift system: Lawrence, University of Kansas, Ph.D. thesis, 430 p.

Szymanski, E., Stockli, S.F., Johnson, P.R., and Hager, C., 2016, Thermochronometric evidence for diffuse extension and two-phase rifting within the Central Arabian margin of the Red Sea Rift: Tectonics, v. 35, p. 2863–2895.

Tesfaye, S., and Ghebreab, W., 2013, Simple shear detachment fault system and marginal grabens in the southernmost Red Sea rift: Tectonophysics, v. 608, p. 1268–1279.

Turcotte, D., and Schubert, G., 2014, Geodynamics (3d ed.): Cambridge University Press, 472 p.

U.S. Geological Survey and Arabian American Oil Company, comp., 1963, Geologic map of the Arabian Peninsula: U.S. Geological Survey Miscellaneous Geological Investigations Map 270–A, scale 1:2,000,000, https://doi.org/10.3133/i270A.

Voggenreiter, W., Hotzl, H., and Mechie, J., 1988, Low-angle detachment origin for the Red Sea Rift system?: Tectonophysics, v. 150, p. 51–75.

Wegener, A., 1929, Die entsehung der kontinente und ozeane (4th ed.) [The origin of continents and oceans; translated by J. Biram, 1966]: New York, Dover Publications, Inc., 246 p.

Wernicke, B., 1985, Uniform-sense normal shear of the continental lithosphere: Canadian Journal of Earth Sciences, v. 22, p. 108–125.

Whitmarsh R.B., Weser, O.E., Ross, D.A., 1974, Initial reports of the deep sea drilling project: Government Printing Office, Washington, v. 23, 1,180 p.

Yao, Z., Mooney, W.D., Zahran, H.M., and Youssef, S.E.H., 2017, Upper mantle velocity structure beneath the Arabian Shield from Rayleigh surface wave tomography and its implications: Journal of Geophysical Research Solid Earth, v. 122, no. 8, p. 6552–6568.

Zumbo, V., Feraud, G., Bertrand, H., and Chazot, G., 1995, $^{40}Ar/^{39}Ar$ chronology of Tertiary magmatic activity in southern Yemen during the early Red Sea-Aden rifting: Journal of Volcanology and Geothermal Resources, v. 65, p. 265–279.

Appendix 1. $^{40}Ar/^{39}Ar$ Analysis Results

This appendix shows the $^{40}Ar/^{39}Ar$ geochronologic results of incremental heating analysis on groundmass concentrates from five Harrat Rahat basalt samples. Full analytical techniques are described by Stelten and others (2023). $^{40}Ar^{*}$ is the percentage of radiogenic argon. Isotope quantities are listed in volts (7.1E−14 moles/volt); they are corrected for extraction line and mass spectrometer background and mass discrimination as well as radioactive decay. Experimental information is provided for each sample (following each table), including the total gas age, weighted mean plateau age and isochron age (and the mean square of weighted deviates [MSWD] for each), and $^{40}Ar/^{36}Ar$ intercept. *J* is the irradiation parameter, monitored by Bodie Hills sanidine with an assigned age of 9.7946 million years (Ma) (Fleck and others, 2019). Ages are given in either thousand years ago (kilo-annum [ka]) or million years ago (mega-annum [Ma]). Reported errors incorporate counting statistics and instrumental corrections, uncertainties on standards, and other sources (Schaen and others, 2021), summed quadratically and reported as 1 standard deviation (1 sigma), unless otherwise noted. Weighted mean age calculations weigh ages from individual increments by the inverse of their errors. A priori errors sum only analytical errors, 1 sigma errors incorporate a measure of the dispersion of the individual increment ages, and 95 percent (%) confidence errors incorporate both the dispersion and the Student's t-value based on the number of steps included in the calculation (Taylor, 1997; Hughes and Hase, 2010).

Basalt Sample R17AC155

Table 1.1. $^{40}Ar/^{39}Ar$ analysis results for basalt sample R17AC155.

[T, temperature; °C, degrees Celsius; Ma, mega-annum; %, percent]

T (°C)	Age (Ma)	% $^{40}Ar^*$	K/Ca	K/Cl	Moles $^{40}Ar^*$	$\sum^{39}Ar$	^{40}Ar	^{39}Ar	^{38}Ar	^{37}Ar	^{36}Ar
550	13.72±0.03	86.07	0.57	−2,635	2.16E−13	0.04	3.531772±0.000983	0.086926±0.000134	0.001311±0.000031	0.080005±0.000857	0.001671±0.000017
600	13.50±0.03	87.23	0.5	−2,251	2.65E−13	0.08	4.276584±0.001171	0.108383±0.000144	0.001562±0.000047	0.114373±0.001161	0.001862±0.000020
650	13.43±0.02	89.54	0.45	−33,494	5.25E−13	0.18	8.243078±0.002492	0.215660±0.000206	0.003352±0.000038	0.252192±0.001619	0.002959±0.000022
700	13.56±0.02	90.63	0.55	−24,119	5.55E−13	0.27	8.599727±0.002578	0.225403±0.000216	0.003432±0.000073	0.216003±0.000993	0.002761±0.000024
750	13.55±0.02	90.31	0.68	−13,471	4.81E−13	0.36	7.492742±0.001902	0.195808±0.000198	0.002969±0.000059	0.151470±0.001599	0.002474±0.000022
800	13.57±0.02	89.67	0.65	−22,170	4.28E−13	0.43	6.712009±0.001876	0.173970±0.000211	0.002690±0.000040	0.141149±0.000838	0.002362±0.000020
850	13.57±0.02	88.02	0.5	−19,674	4.26E−13	0.51	6.796095±0.001929	0.172897±0.000207	0.002748±0.000056	0.181006±0.000404	0.002779±0.000022
900	13.55±0.03	84.27	0.52	−81,035	3.24E−13	0.56	5.407772±0.001933	0.131956±0.000137	0.002263±0.000043	0.132665±0.000888	0.002886±0.000023
975	13.28±0.03	84.61	0.84	−3,721	3.41E−13	0.62	5.667778±0.001651	0.141690±0.000223	0.002247±0.000054	0.088256±0.001190	0.002946±0.000026
1,050	13.09±0.02	89.04	0.99	−4,403	3.76E−13	0.69	5.930787±0.001834	0.158241±0.000212	0.002334±0.000065	0.083456±0.000629	0.002200±0.000022
1,125	13.03±0.02	85.06	0.45	−67,173	6.95E−13	0.82	11.397391±0.003424	0.291869±0.000280	0.004891±0.000063	0.343040±0.001268	0.005800±0.000029
1,175	13.18±0.02	79.33	0.18	6,505	5.35E−13	0.92	9.482388±0.003015	0.224181±0.000224	0.004336±0.000055	0.657583±0.001588	0.006751±0.000031
1,225	13.30±0.03	73.57	0.03	4,263	3.42E−13	0.98	6.534502±0.003520	0.143375±0.000167	0.003162±0.000045	2.301893±0.002727	0.006430±0.000029
1,300	13.33±0.09	72.46	0.03	4,771	6.38E−14	0.99	1.238345±0.000634	0.026776±0.000064	0.000602±0.000031	0.532814±0.002847	0.001292±0.000017
1,375	13.26±0.10	74.31	0.03	1,776	4.88E−14	1	0.922039±0.000430	0.020522±0.000059	0.000476±0.000027	0.382160±0.001254	0.000901±0.000015
1,450	13.56±0.19	73.16	0.02	−2,976	2.22E−14	1	0.423777±0.000324	0.009104±0.000053	0.000183±0.000030	0.198935±0.001653	0.000437±0.000013

Packet IRR364-YX, experiment #17Z0187, 0.1573 grams basalt, all errors ±1 sigma
J = 0.000218119041±0.000000462613
Calculated bulk K/Ca = 0.208±0.092, calculated K_2O = 1.86 weight percent, calculated CaO = 10.92 weight percent
Total gas age = 13.38±0.03 Ma

Weighted mean plateau age = 13.56±0.03 Ma (±1 sigma, including ±J), 38.7 percent ^{39}Ar released
Weighted mean plateau age = 13.56±0.03 Ma (a priori, including ±J), 38.7 percent ^{39}Ar released
Weighted mean plateau age = 13.56±0.03 Ma (95 percent confidence, including ±J)
MSWD = 0.20 (Good fit, MSWD < 2.77)
Steps 5 of 16 (700, 750, 800, 850, 900 °C)

Isochron age = 13.58±0.05 Ma (±1 sigma, including ±J)
Isochron age = 13.58±0.05 Ma (a priori errors, including ±J)
Isochron age = 13.58±0.10 Ma (95 percent confidence, including ±J)
MSWD = 0.23 (Good fit, MSWD < 3.12)
$^{40}Ar/^{36}Ar$ intercept = 296.0±7.6 (±1 sigma)
$^{40}Ar/^{36}Ar$ intercept = 296.0±7.6 (a priori)
$^{40}Ar/^{36}Ar$ intercept = 296.0±16.4 (95 percent confidence)
Steps 5 of 16 (700, 750, 800, 850, 900 °C)

Basalt Sample R17AC157

Table 1.2. $^{40}Ar/^{39}Ar$ analysis results for basalt sample R17AC157.

[T, temperature; °C, degrees Celsius; Ma, mega-annum; %, percent]

T (°C)	Age (Ma)	% $^{40}Ar^*$	K/Ca	K/Cl	Moles $^{40}Ar^*$	$\Sigma^{39}Ar$	^{40}Ar	^{39}Ar	^{38}Ar	^{37}Ar	^{36}Ar
400	12.05±0.19	73.27	0.65	14,262	1.05E−14	0.01	0.201597±0.000230	0.004782±0.000024	0.000098±0.000016	0.003831±0.000876	0.000182±0.000008
475	12.05±0.03	78.67	0.5	1,560	1.60E−13	0.1	2.861527±0.001116	0.072903±0.000139	0.001542±0.000029	0.077038±0.001337	0.002066±0.000016
550	12.77±0.02	78.58	0.59	861	3.86E−13	0.3	6.910694±0.002104	0.165883±0.000185	0.003936±0.000078	0.147409±0.001667	0.004999±0.000023
600	13.29±0.03	80.82	0.99	802	2.93E−13	0.45	5.094030±0.001884	0.120811±0.000172	0.002847±0.000062	0.064100±0.001043	0.003290±0.000022
650	13.38±0.03	76.36	0.89	1,280	2.57E−13	0.58	4.732636±0.001714	0.105333±0.000168	0.002439±0.000024	0.062329±0.001403	0.003765±0.000020
700	13.49±0.03	72.34	0.72	1,696	2.20E−13	0.68	4.265789±0.001456	0.089183±0.000110	0.002138±0.000050	0.064879±0.001398	0.003971±0.000021
750	13.55±0.04	71.87	0.77	2,060	1.56E−13	0.76	3.050236±0.000955	0.063086±0.000104	0.001499±0.000026	0.043154±0.001276	0.002886±0.000020
800	13.48±0.06	71.49	1.16	12,566	1.11E−13	0.82	2.182056±0.000952	0.045112±0.000094	0.000998±0.000031	0.020452±0.000894	0.002090±0.000018
875	12.98±0.04	73.41	0.79	5,764	1.66E−13	0.9	3.184069±0.001006	0.070234±0.000097	0.001506±0.000025	0.046370±0.001128	0.002849±0.000019
925	12.03±0.06	61.5	0.17	−18,815	9.28E−14	0.96	2.120573±0.001166	0.042354±0.000106	0.001061±0.000030	0.129620±0.001596	0.002771±0.000020
1,000	11.90±0.09	45.42	0.02	1,304	7.89E−14	1	2.440920±0.000917	0.036974±0.000089	0.001461±0.000045	0.900299±0.003668	0.004715±0.000025

Packet IRR366-BB, experiment #18Z0023, 0.0917 grams basalt, all errors ±1 sigma
J = 0.000216848836±0.000000240627
Calculated bulk K/Ca = 0.274±0.165, calculated K_2O = 1.12 weight percent, calculated CaO = 5.01 weight percent
Total gas age = 12.98±0.02 Ma

Weighted mean plateau age = 13.41±0.07 Ma (±1 sigma, including ±J), 51.9 percent ^{39}Ar released
Weighted mean plateau age = 13.41±0.02 Ma (a priori, including ±J), 51.9 perecnt ^{39}Ar released
Weighted mean plateau age = 13.41±0.15 Ma (95% confidence, including ±J)
MSWD = 9.33 (poor fit, MSWD > 2.77)
Steps 5 of 11 (600, 650, 700, 750, 800 °C)

Isochron age = 12.95±0.08 Ma (±1 sigma, including ±J)
Isochron age = 12.95±0.08 Ma (a priori errors, including ±J)
Isochron age = 12.95±0.19 Ma (95 percent confidence, including ±J)
MSWD = 0.41 (good fit, MSWD < 3.12)
$^{40}Ar/^{36}Ar$ intercept = 330.3±5.6 (±1 sigma)
$^{40}Ar/^{36}Ar$ intercept = 330.3±5.6 (a priori)
$^{40}Ar/^{36}Ar$ intercept = 330.3±12.9 (95 percent confidence)
Steps 5 of 11 (600, 650, 700, 750, 800 °C)

Basalt Sample R17AC158

Table 1.3. $^{40}Ar/^{39}Ar$ analysis results for basalt sample R17AC158.

[T, temperature; °C, degrees Celsius; Ma, mega-annum; %, percent]

T (°C)	Age (Ma)	% $^{40}Ar^*$	K/Ca	K/Cl	Moles $^{40}Ar^*$	$\sum^{39}Ar$	^{40}Ar	^{39}Ar	^{38}Ar	^{37}Ar	^{36}Ar
450	13.64±0.12	79.42	−0.1	2,794	2.46E−14	0.01	0.434681±0.000350	0.009813±0.000045	0.000199±0.000021	−0.040950±0.001179	0.000288±0.000008
525	12.33±0.03	78.29	0.72	19,279	1.82E−13	0.12	3.272528±0.001100	0.080872±0.000106	0.001527±0.000024	0.058918±0.000486	0.002396±0.000019
575	12.37±0.03	68.56	0.76	−7,544	2.60E−13	0.26	5.321499±0.001994	0.114847±0.000177	0.002493±0.000050	0.079146±0.001822	0.005627±0.000028
625	12.24±0.05	55.28	0.8	29,187	2.32E−13	0.39	5.892393±0.001720	0.103549±0.000161	0.003027±0.000069	0.068030±0.001416	0.008845±0.000038
675	12.54±0.06	51.35	0.79	−3,809	2.00E−13	0.51	5.462642±0.001502	0.087073±0.000177	0.002712±0.000055	0.057839±0.002542	0.008918±0.000042
725	12.74±0.05	54.58	0.65	−9,231	1.70E−13	0.6	4.374533±0.001400	0.072945±0.000106	0.002170±0.000050	0.059003±0.002435	0.006672±0.000031
800	12.72±0.05	60.72	0.53	−5,074	1.77E−13	0.7	4.104794±0.001164	0.076256±0.000117	0.001949±0.000044	0.075555±0.001677	0.005422±0.000027
875	12.65±0.05	74.79	0.58	22,614	1.35E−13	0.77	2.527987±0.000962	0.058192±0.000123	0.001176±0.000033	0.052494±0.001399	0.002149±0.000020
950	12.31±0.04	80.33	0.49	2,483	1.24E−13	0.84	2.167953±0.000664	0.055098±0.000097	0.001088±0.000033	0.059228±0.002110	0.001445±0.000014
1,025	11.86±0.04	71.76	0.18	1,641	1.67E−13	0.94	3.276913±0.000955	0.077317±0.000116	0.001802±0.000037	0.224572±0.001294	0.003162±0.000022
1,100	11.23±0.09	57.33	0.04	828	5.42E−14	0.97	1.327476±0.000504	0.026661±0.000095	0.000851±0.000033	0.390626±0.003147	0.002007±0.000019
1,200	11.69±0.11	58.19	0.03	563	4.47E−14	1	1.080125±0.000418	0.021209±0.000086	0.000731±0.000035	0.412876±0.004613	0.001629±0.000016

Packet IRR366-BC, experiment #18Z0020, 0.1063 grams basalt, all errors ±1 sigma
J = 0.000216406307±0.000000293269
Calculated bulk K/Ca = 0.274±0.118, calculated K_2O = 0.93 weight percent, calculated CaO = 4.16 weight percent
Total gas age = 12.36±0.02 Ma

Weighted mean plateau age = 12.33±0.04 Ma (±1 sigma, including ±J), 38.2 percent ^{39}Ar released
Weighted mean plateau age = 12.33±0.03 Ma (a priori, including ±J), 38.2 percent ^{39}Ar released
Weighted mean plateau age = 12.33±0.09 Ma (95 percent confidence, including ±J)
MSWD = 2.19 (good fit, MSWD < 3.69)
Steps 3 of 12 (525, 575, 625 °C)

Isochron age = 12.40±0.08 Ma (±1 sigma, including ±J)
Isochron age = 12.4±0.1 Ma (a priori errors, including ±J)
Isochron age = 12.4±0.2 Ma (95 percent confidence, including ±J)
MSWD = 2.11 (good fit, MSWD < 5.02)
$^{40}Ar/^{36}Ar$ intercept = 294.6±3.7 (±1 sigma)
$^{40}Ar/^{36}Ar$ intercept = 294.6±2.6 (a priori)
$^{40}Ar/^{36}Ar$ intercept = 294.6±8.5 (95 percent confidence)
Steps 3 of 12 (525, 575, 625 °C)

Basalt Sample R17JRD10

Table 1.4. $^{40}Ar/^{39}Ar$ analysis results for basalt sample R17JRD10.

[T, temperature; °C, degrees Celsius; ka, kilo-annum; %, percent]

T (°C)	Age (ka)	% $^{40}Ar^*$	K/Ca	K/Cl	Moles $^{40}Ar^*$	$\sum^{39}Ar$	^{40}Ar	^{39}Ar	^{38}Ar	^{37}Ar	^{36}Ar
450	3,807.36±375.73	47.78	0.08	−112	1.85E−15	0.01	0.054430±0.000317	0.002689±0.000041	−0.000049±0.000013	0.018158±0.001015	0.000100±0.000008
525	3,244.77±76.84	58.62	0.09	−313	1.19E−14	0.09	0.285403±0.000718	0.020285±0.000063	0.000066±0.000039	0.119859±0.001884	0.000429±0.000013
575	2,938.23±40.78	61.5	0.12	10,4891	1.64E−14	0.2	0.372178±0.000316	0.030618±0.000079	0.000497±0.000016	0.138618±0.002138	0.000519±0.000010
625	2,918.38±32.63	62.4	0.15	14,418	1.93E−14	0.34	0.434211±0.000259	0.036463±0.000101	0.000595±0.000026	0.128041±0.001210	0.000583±0.000010
675	2,905.36±42.79	63.51	0.16	8,035	1.77E−14	0.47	0.392157±0.000274	0.033665±0.000101	0.000552±0.000025	0.109984±0.001119	0.000510±0.000012
725	2,944.60±45.78	56.11	0.14	15,722	1.51E−14	0.58	0.377385±0.000293	0.028247±0.000080	0.000485±0.000026	0.102357±0.001516	0.000584±0.000011
775	3,028.42±58.26	49.29	0.13	−2,970	1.24E−14	0.66	0.353533±0.000264	0.022610±0.000072	0.000379±0.000016	0.093666±0.000988	0.000627±0.000011
825	2,948.36±79.42	45.49	0.11	−2,454	8.96E−15	0.73	0.276886±0.000239	0.016796±0.000051	0.000288±0.000028	0.081552±0.001729	0.000528±0.000011
900	2,996.40±86.54	38.84	0.1	2,529	8.08E−15	0.78	0.292572±0.000275	0.014912±0.000054	0.000335±0.000025	0.077957±0.001126	0.000621±0.000011
975	3,048.66±108.65	40.18	0.09	2,633	7.02E−15	0.83	0.245437±0.000182	0.012727±0.000054	0.000282±0.000012	0.076195±0.002610	0.000513±0.000012
1,050	2,966.03±106.24	28.68	0.06	−9,799	7.94E−15	0.89	0.389273±0.000258	0.014841±0.000055	0.000365±0.000017	0.131342±0.001768	0.000967±0.000013
1,150	2,898.47±109.87	15.01	0.01	1,389	1.18E−14	0.97	1.104699±0.000366	0.023057±0.000056	0.000982±0.000037	0.909989±0.006418	0.003400±0.000020
1,250	3,079.46±178.04	23.94	0.01	730	4.22E−15	1	0.245994±0.000230	0.007761±0.000038	0.000272±0.000024	0.377997±0.002181	0.000733±0.000011

Packet IRR366-BA, experiment #18Z0024, 0.1043 grams basalt, all errors ±1 sigma
J = 0.000217368±2.12E−07
Calculated bulk K/Ca = 0.058±0.026, calculated K_2O = 0.32 weight percent, calculated CaO = 6.68 weight percent
Total gas age = 2,983.54±19.77 ka

Weighted mean plateau age = 2,942.70±17.29 ka (±1 sigma, including ±J), 91.3 percent ^{39}Ar released
Weighted mean plateau age = 2,942.70±17.29 ka (a priori, including ±J), 91.3 percent ^{39}Ar released
Weighted mean plateau age = 2,942.70±28.58 ka (95 percent confidence, including ±J)
MSWD = 0.56 (good fit, MSWD < 2.05)
Steps 11 of 13 (575, 625, 675, 725, 775, 825, 900, 975, 1,050, 1,150, 1,250 °C)

Isochron age = 2,931.44±25.48 ka (±1 sigma, including ±J)
Isochron age = 2,931.44±25.48 ka (a priori errors, including ±J)
Isochron age = 2,931.44±56.48 ka (95 percent confidence, including ±J)
MSWD = 0.58 (Good fit, MSWD < 2.11)
$^{40}Ar/^{36}Ar$ intercept = 299.6±2.0 (±1 sigma)
$^{40}Ar/^{36}Ar$ intercept = 299.6±2.0 (a priori)
$^{40}Ar/^{36}Ar$ intercept = 299.6±4.5 (95 percent confidence)
Steps 11 of 13 (575, 625, 675, 725, 775, 825, 900, 975, 1,050, 1,150, 1,250 °C)

Basalt Sample R 17TS219

Table 1.5. $^{40}Ar/^{39}Ar$ analysis results for basalt sample R17TS219.

[T, temperature; °C, degrees Celsius; ka, kilo-annum; %, percent]

T (°C)	Age (ka)	% $^{40}Ar^*$	K/Ca	K/Cl	Moles $^{40}Ar^*$	$\Sigma^{39}Ar$	^{40}Ar	^{39}Ar	^{38}Ar	^{37}Ar	^{36}Ar
550	2,321.50±49.16	62.37	0.55	−1,679	1.35E−14	0.03	0.304600±0.000313	0.031973±0.000079	0.000411±0.000025	0.030699±0.000516	0.000393±0.000013
625	2,298.93±34.47	77.99	0.44	−822	2.84E−14	0.09	0.511592±0.000911	0.067823±0.000126	0.000610±0.000052	0.081202±0.000702	0.000400±0.000020
700	2,183.55±31.62	34.2	0.32	−437	5.96E−14	0.23	2.450335±0.003721	0.150034±0.000361	0.001513±0.000162	0.243921±0.001522	0.005469±0.000038
750	2,162.66±35.76	35.97	0.2	−552	4.04E−14	0.33	1.577042±0.002081	0.102604±0.000223	0.001190±0.000098	0.264895±0.001566	0.003457±0.000030
800	2,132.44±34.16	54.08	0.36	−1,596	3.14E−14	0.41	0.815573±0.001094	0.080842±0.000157	0.001082±0.000062	0.118493±0.000630	0.001288±0.000023
875	2,176.45±28.60	62.58	0.43	−1,552	3.57E−14	0.49	0.800777±0.000648	0.089983±0.000125	0.001124±0.000058	0.110128±0.000587	0.001034±0.000022
950	2,156.82±28.00	57.32	0.36	−3,573	3.48E−14	0.57	0.848145±0.000567	0.088106±0.000136	0.001282±0.000042	0.127937±0.000591	0.001248±0.000021
1,050	2,140.91±27.24	54.06	0.27	−37,874	3.49E−14	0.66	0.907059±0.000509	0.089557±0.000130	0.001432±0.000044	0.171148±0.000867	0.001444±0.000021
1,125	2,143.22±24.11	56.65	0.23	20,056	4.12E−14	0.75	1.016079±0.000447	0.105036±0.000153	0.001684±0.000053	0.238277±0.001527	0.001542±0.000021
1,175	2,139.86±25.52	40.7	0.09	2,534	3.70E−14	0.84	1.276464±0.000452	0.095197±0.000152	0.001898±0.000057	0.551907±0.004398	0.002690±0.000020
1,225	2,231.77±31.94	32.68	0.04	−31,120	4.38E−14	0.94	1.885135±0.000706	0.108906±0.000145	0.002248±0.000033	1.575273±0.002529	0.004693±0.000028
1,325	2,255.94±45.57	39.72	0.04	−3,599	2.05E−14	0.99	0.724484±0.000416	0.050333±0.000150	0.000893±0.000053	0.732636±0.001359	0.001668±0.000019
1,425	2,311.21±164.40	42.36	0.03	3,014	3.91E−15	1	0.129867±0.000212	0.009407±0.000039	0.000187±0.000023	0.158254±0.000589	0.000295±0.000013

Packet IRR364-YU, experiment #17Z0194, 0.1504 grams basalt, all errors ±1 sigma
J = 0.000216590025±0.000000350012
Calculated bulk K/Ca = 0.127±0.055, calculated K_2O = 0.90 weight percent, calculated CaO = 8.65 weight percent
Total gas age = 2,184.28±9.98 ka

Weighted mean plateau age = 2,153.08±10.71 ka (±1 sigma, including ±J), 75.0 percent ^{39}Ar released
Weighted mean plateau age = 2,153.08±10.71 ka (A priori, including ±J), 75.0 percent ^{39}Ar released
Weighted mean plateau age = 2,153.08±14.61 ka (95 percent confidence, including ±J)
MSWD = 0.38 (good fit, MSWD < 2.29)
Steps 8 of 13 (700, 750, 800, 875, 950, 1,050, 1,125, 1,175 °C)

Isochron age = 2,139.97±26.08 ka (±1 sigma, including ±J)
Isochron age = 2,139.97±26.08 ka (a priori errors, including ±J)
Isochron age = 2,139.97±57.69 ka (95 percent confidence, including ±J)
MSWD = 0.40 (good fit, MSWD < 2.40)
$^{40}Ar/^{36}Ar$ intercept = 300.2±3.1 (±1 sigma)
$^{40}Ar/^{36}Ar$ intercept = 300.2±3.1 (a priori)
$^{40}Ar/^{36}Ar$ intercept = 300.2±6.8 (95 percent confidence)
Steps 8 of 13 (700, 750, 800, 875, 950, 1,050, 1,125, 1,175 °C)

References Cited

Fleck, R.J., Calvert, A.T., Coble, M.A., Wooden, J.L., Hodges, K., Hayden, L.A., van Soest, M.C., du Bray, E.A., and John, D.A., 2019, Characterization of the rhyolite of Bodie Hills and $^{40}Ar/^{39}Ar$ intercalibration of Ar mineral standards: Chemical Geology, v. 525, p. 282–302.

Hughes, I.G., and Hase, T.P.A., 2010, Measurements and their uncertainties—A practical guide to modern error analysis: Oxford University Press, 136 p.

Schaen, A.J., Jicha, B.R., Hodges, K.V., Vermeesch, P., Stelten, M.E., Mercer, C.M., Phillips, D., Rivera, T.A., Jourdan, F., Matchan, E.L., Hemming, S.R., Morgan, L.E., Kelley, S.P., Cassata, W.S., Heizler, M.T., Vasconcelos, P.M., Benowitz, J.A., Koppers, A.P., Mark, D.F., Niespolo, E.M., Sprain, C.J., Hames, W.E., Kuiper, K.F., Turrin, B.D., Renne, P.R., Ross, J., Nomade, S., Guillou, H., Webb, L.E., Cohen, B.A., Calvert, A.T., Joyce, N., Ganerød, M., Wijbrans, J., Ishizuka, O., He, H., Ramirez, A., Pfänder, J.A., Lopez-Martínez, M., Qiu, H., and Singer, B.S., 2021, Interpreting and reporting $^{40}Ar/^{39}Ar$ geochronologic data: Geological Society of America Bulletin, v. 133, no. 3–4, p. 461–487.

Stelten, M.E., Downs, D.T., Champion, D.E., Dietterich, H.R., Calvert, A.T., Sisson, T.W., Mahood, G.A., and Zahran, H.M., 2023, Eruptive history of northern Harrat Rahat—Volume, timing, and composition of volcanism over the past 1.2 million years, chap. D *of* Sisson, T.W., Calvert, A.T., and Mooney, W.D., eds., Active volcanism on the Arabian Shield—Geology, volcanology, and geophysics of northern Harrat Rahat and vicinity, Kingdom of Saudi Arabia: U.S. Geological Survey Professional Paper 1862 [also released as Saudi Geological Survey Special Report SGS–SP–2021–1], 46 p., https://doi.org/10.3133/pp1862D.

Taylor, J.R., 1997, An introduction to error analysis—The study of uncertainties in physical measurements (2d ed.): Sausalito, Calif., University Science Books, 327 p.

Moffett Field Publishing Service Center, California
Manuscript approved February 20, 2022
Edited by Monica Erdman
Layout and design by Kimber Petersen
Illustration support by Katie Sullivan

Calvert and Sisson—**Cenozoic Tectonics of the Western Arabia Plate near Al Madīnah, Kingdom of Saudi Arabia**—Professional Paper 1862–B

ISSN 1044-9612 (print)
ISSN 2330-7102 (online)
https://doi.org/10.3133/pp1862B